Microstructure, mechanical behavior, and crystallographic texture in a hot forged dual-phase stainless steel

Riad Badji, Bellel Cheniti, Charlie Kahloun, Thierry Chauveau, Mohammed Hadji, Brigitte Bacroix

Microstructure, Mechanical Behavior and Crystallographic Texture in a Hot Forged Dual Phase Stainless Steel.

Riad Badji (riadbadji@gmail.com)
Centre de Recherche en Technologies Industrielles https://orcid.org/0000-0002-7432-7992
Bellel Cheniti
Université Sorbonne Paris Nord
Charlie Kahloun
Université Sorbonne Paris Nord
Thierry Chauveau
Université Sorbonne Paris Nord
Mohammed Hadji
University of Blida
brigitte Bacroix
Université Sorbonne Paris Nord

Research Article

Keywords: Duplex stainless steel, hot forging, microstructure, mechanical behavior, crystallographic texture

Posted Date: March 16th, 2021

DOI: https://doi.org/10.21203/rs.3.rs-295369/v1

Microstructure, mechanical behavior and crystallographic texture in a hot forged dual phase stainless steel.

Riad Badji[1], Bellel Cheniti[1], Charlie Kahloun[2], Thierry Chauveau[2], Mohammed Hadji [3], Brigtte Bacroix[2]

[1]Research Centre in Industrial Technologies CRTI, P.O. Box 64, Chéraga. Algeria.

[2]LSPM – CNRS, Université Sorbonne Paris Nord, 93430 Villetaneuse, France

[3] Laboratoire d'étude et de Recherche en Technologies Industrielles, University of Blida 1, Blida, Algeria.

Corresponding author : Rad BADJI, tel : +213 23 11 59 35.

e-mail 1 : r.badji@crti.dz, e-mail2 : riadbadji@gmail.com,

Abstract:

In this work, the hot forging behavior of a dual phase stainless steel in the temperature range of 850 – 1250 °C was investigated. The study revealed the occurrence of a significant cracking phenomenon for processing temperatures below 950 °C that was attributed to the combined effect of intermetallic precipitation and severe deformation. EBSD examination highlighted the occurrence of continuous dynamic recrystallization in both ferrite and austenite microstructures for processing temperatures above 1050 °C. Increasing the hot forging temperature to 1250 °C increased the low angle grain boundaries fraction and lowered the one of the high angle grain boundaries. This was accompanied by a gradual change in the crystallographic texture of the material. The mechanical behavior investigation showed that the steel plasticity, sharply dropped after forging at 850°, was gradually recovered after hot forging at temperatures above 1050°C. This was confirmed by nanoindentation measurements that revealed a remarkable increase of the hardness and young modulus of the steel after hot forging at 850°C and 950°C due to the dislocation nucleation and the σ phase precipitation at γ/δ interface. The enhancement of dislocation movement at the vicinity of the grain boundaries due to the absence of σ phase as well as the dynamic recovery and recrystallization occurring in the temperature range of 1050°C - 1250 °C improved the global mechanical properties of the hot forged steel.

Key words: Duplex stainless steel; hot forging ; microstructure; mechanical behavior; crystallographic texture.

1. Introduction

During industrial fabrication processes, metallic materials undergo various microstructural transformations due to the thermal, mechanical or thermomechanical effect of the process. The resulting microstructural changes within the material often constitute a source of stress/strain incompatibilities that can cause its damage. Among the wide range of metallic materials, duplex stainless steels (DSS) are characterized by a dual phase microstructure constituted of austenite (γ) and ferrite (δ). Their combination of high mechanical properties and improved corrosion resistance makes them excellent choices for applications in several industrial domains such as petroleum, gas and petrochemical industries [1-5]. In order to fabricate some specific components, DSS are hot processed by rolling or forging. However, particular attention should be given to the hot processing of these materials due to the complex microstructural evolutions that can take place such as precipitation of intermetallic phases if the deformation temperature is not well controlled. Indeed, different evolutions of the hardening state have been reported in austenite and ferrite during hot processing of DSS [1-2]. The ferrite is often reported to soften during hot forging by dynamic recovery (DRV) whereas dynamic recrystallization (DRX) is reported to occur preferentially in austenite [6-7]. Both DRV and DRX intensities are related to the stacking fault energy (SFE) that controls the ability of dislocations to rearrange by cross slip or by climb. [4-8]. More generally, since austenite and ferrite phases have different elastic and plastic properties in addition to different thermal expansion coefficients, they should act differently during a deformation process. The microstructural and associated hardening evolutions that take place during the hot deformation of single phase austenitic and ferritic stainless steels have been extensively investigated in several research works [7-12]. It was already concluded that easy dislocation annihilation and rearrangement, leading to dynamic recovery, occurs in ferrite. On the other hand, the low stacking fault energy of austenite weakens the dislocation mobility and limits the occurrence of DRV. Consequently, DRX occurs once a critical strain constituting a driving force for the nucleation of new grains is achieved. Nevertheless, some researchers [4] mentioned that even for materials having high SFE, it was possible to create some experimental conditions that could delay DRV and favor the occurrence of DRX. The situation becomes even more complex when the two phases are deformed simultaneously like in a dual phase stainless steel due to a non-uniform deformation or stress repartition between its constituent phases. Cizek and Wynne [4] revealed the occurrence of extended DRV in both phases of a

DDS hot deformed by torsion. Their results are in agreement with those published by Blancin et al. [13] who also highlighted the dissimilarity of the plastic properties of a hot deformed DSS. Later, Duprez et al. [14] studied the flow behavior of a hot deformed DSS and observed an enhanced ductility that was correlated to the amount of dynamic softening caused by the DRX of austenite. On the other hand, Iza Mendia [6] reported the suppression of DRX during hot processing of DSS and confirmed the dependence of its mechanical behavior on the initial microstructure. Similarly, DRX was observed by Dehghan-Manshadi et al. [15] whereas Fan et al. [16] demonstrated the occurrence of only DRV in austenite and DRX in ferrite of an as casted hot deformed DSS. The effect of the crystallographic texture developed during the thermomechanical processing of DSS on their final properties was also investigated in the literature. Ul-Haq et al. [17] reported that the ferrite crystallographic texture formed by hot rolling in a DSS consisted of α fiber whereas the austenite one contained Copper and Brass components (see Section 3 for the description of preferred orientations). For Padilha et al. [18] and Cizeck et al. [19] however, the austenite texture in a hot processed DSS appears to be dominated by the Cube and Brass components. Patra et al. [20] investigated the crystallographic texture evolution during thermomechanical processing of a lean DSS. They pointed out that the ferrite was dominated by the Cube and rotated Cube components whereas austenite was mainly characterized by deformation textures such as Copper, Brass and rotated Goss. Recently, Moura et al. [21] concluded that both ferrite and austenite exhibit texture heterogeneities due to the complexity of the thermomechanical process.

As it can be seen, the literature reports a great number of research works dealing with the hot deformation behavior of DSS such as hot rolling, hot torsion, and compression. It should be mentioned though, that the observed softening mechanisms and texture evolutions are still quite dispersed, which tends to underline the important role of the initial microstructure and of some critical parameters of the thermomechanical processing on the resulting characteristics of the material. On the other side and in spite of its industrial importance, the hot forging behavior of DSS is much less documented. In piping industry for example, this process is widely applied to DSS to fabricate pipe connections, flanges, forged discs…, etc. The main objective of this work is thus to study the hot forging behavior of a 2205 DSS in the temperature range varying from 800 to 1250 C°. The microstructure and

crystallographic texture evolutions are presented and discussed based on the expected recrystallization mechanisms that are briefly recalled. Finally, the mechanical behavior is studied through tension and nanoindentation tests.

2. Material and experimental procedure.

A 2205 DSS received in the form of sheets of 10 mm thick with the chemical composition given in Table 1 was used in this work. Samples of 140x30x10mm were machined and prepared for the hot forging process. The hot forging operation was conducted at temperatures ranging from 850°C to 1250°C. For each forging temperature, the samples were heated for 1h, then taken separately and forged immediately in a 50T press. For each temperature, forging was carried out in five passes. Due to the very high strain rate (about 1s-1), the duration of each deformation step was estimated to be between 10 and 20 times shorter than the interpass time, which varied between 12 and 19 seconds for all processed samples and all temperatures. The characterization of the material after hot deformation was firstly done by X-Ray diffraction using an INEL Equinox 1000 diffractometer equipped with a linear detector and a cobalt long fine focus X-ray source ($\Delta 2\theta = 0.03^\circ$, $\lambda = 1.78898$Å, $\omega \neq \theta$). Microstructural examination was then done using a Nikon optical microscope and a ZEISS Gemini SEM 300 scanning electron microscope equipped with EDS system. Global crystallographic texture of each phase was characterized using X-Ray diffraction. Quantitative Texture Analysis (QTA) was performed using an INEL 4 circles diffractometer in Bragg-Brentano geometry with a cobalt point focus X ray source ($\lambda = 1.7902$Å, with 2/3 $K\alpha_1$ and 1/3 $K\alpha_1$ radiations). The measured pole figures (with a maximum tilt angle of 80°) are 200, 220 and 111 for the BCC phase and 111, 200 and 220 for the FCC one.

Table 1: Chemical composition of the investigated 2205 DSS.

Element	C	Si	Mn	Ni	Mo	Cr	P	S	Cu	N
(Wt. %)	0.029	0.28	1.20	5.03	2.21	22.04	0.017	0.014	0.22	0.12

The determination of the Orientation Distribution Function (ODF) and complete pole figures were calculated using Labotex© software. Micro-texture analysis was done using EBSD attached to the SEM cited above equipped with the automatic Orientation Imaging Microscopy (OIM®) software from Tex-SEM laboratories Inc. Scans of 400 µm × 400 µm were performed with a step of 0.5 µm. For both EBSD and X-ray techniques, texture measurements were performed on the plane perpendicular to the normal direction (ND) of the specimens, with the initial rolling direction (RD) of the sheet taken as reference direction. For this purpose, the specimens were mechanically polished with silicon carbide paper up to grade 4000, and then with diamond paste (1 and 0.25 µm) on polishing clothes. Finally, they were electropolished using the A2 Struers solution. From the EBSD data, the Grain Average Misorientation (GAM) – i.e. the misorientation between each neighbouring pair of points within the grain, averaged on all points belonging to one given grain – was calculated. This parameter, which is considered to be much less sensitive to the grain size than other parameters such as the Grain Orientation Spread (GOS) has been recently shown to be well suited to characterize in details the recrystallized state of a hot forged Ni based alloy. [22] The area percentage occupied by grains associated with a given GAM value was then calculated to get GAM distributions. Deformed materials are usually characterized by high GAM values due to their high dislocation density whereas recrystallized ones exhibit much weaker GAM values due to their low dislocation density – typically below 1° [22, 23]. For the present analysis, the misorientation separating grain boundaries (GB) from sub-grain boundaries (SGB) has also been set to 15° and the percentages of Low Angle Grain Boundaries (LAGB, misorientation <15°) and High Angle Grain Boundaries (HAGB, misorientation ≥15°) have also been evaluated in both phases.

For mechanical testing, tensile specimens were machined according to ASTM E8 standard. [24] The specimens were machined with the tensile load direction parallel to the initial rolling direction of the material. The tensile tests were conducted at room temperature at a strain rate of 0.5×10^{-3} s^{-1}.To quantify the local mechanical properties of each individual phase of the hot forged samples at small length scale, nanoindentation measurements were conducted using an Anton Paar NHT-3 nanoindenter with a Berkovich tip under 10 mN load and 1 $mN.s^{-1}$ loading rate. Prior nanoindentation tests, the tip was calibrated using fused silica and the hardness (H_{IT}) and elastic modulus (E_{IT}) were calculated according to

the method proposed by Oliver and Pharr [25]. To ensure the reproducibility of the obtained results, at least 15 indents were performed in each phase.

3. The expected recrystallization mechanisms and resulting textures

Before examining the microstructures, it is worth recalling briefly the expected types of recrystallization mechanisms [26, 27]. These are:

- Dynamic Recovery (DRV), already mentioned as a major mechanism in ferrite during hot deformation (see Section 1): the dislocations, produced continuously during strain, re-organize also continuously under the action of cross-slip and climb and tend to form well-defined structures. The percentages of LAGBs as well as the one of GAM increase. But neither GB migration (GBM) nor nucleation of new grains is observed. As a consequence, the crystal orientation changes are only due to plastic deformation, which can also further increase the degree of grain fragmentation.
- Continuous Dynamic Recrystallization (CDRX): this mechanism is in fact quite close to DRV. The grains fragment continuously under the simultaneous action of dislocation cell formation and reorientation due to plastic strain. Some limited grain growth (GG) can also be observed. Again, the texture evolution is mainly due to re-orientation during plastic strain in this case, slightly altered by the fragmentation of the grains.
- Discontinuous Dynamic Recrystallization (DDRX), usually observed in the austenite (see Section 1): in that case, nucleation and growth of new grains is observed. In most cases, DRV is very limited or completely absent beforehand, and strain provides the necessary driving force for nucleation and further growth. As nuclei are usually formed at GB (often from the bulging of one part of GB), this gives rise to so-called necklace structures. Texture evolution is then more important in that case, mainly due to the growth of the newly formed grains.
- Post Dynamic Recrystallization (PDRX), taking place during the interpass times. This type of recrystallization may occur through classical recrystallization, i.e., nucleation and growth of new grains (this is then equivalent to static recrystallization and sometimes called Post-Static Recrystallization, PSRX) or just through the growth of the grains created by DDRX (this is then called Meta-Dynamic Recrystallization, MDRX). In that last case, no incubation time is needed

then, unlike in the case of PSRX, and this process, associated with limited texture evolution, is then expected to be active during long interpass durations at high temperature.

For the expected textures after hot forging, as the textures of the initial material are quite pronounced (see below) and as most of the main components characterizing the hot rolled and annealed textures are expected to be more or less stable during further compression, we can first recall the main components found in ferrite and austenite after classical rolling and annealing. It is well known that most of the main orientations usually found after rolling and annealing in both phases of the DSS can be grouped into one single section of the Euler space namely the $\varphi_2 = 45°$ one. These orientations, characterized by the classical Miller indices {hkl}<uvw>, where {hkl} and <uvw> are the indices of the rolling plane and direction respectively, are presented in Fig. 1. During hot forging, the initial textures of the two phases will be modified under the simultaneous influence of 3 main important items: (i) the possible activation of high temperature deformation systems, not documented for such high temperatures, but generally not associated with the appearance of radically new orientations [28], (ii) the precise imposed macroscopic boundary conditions, which are not trivial to assess precisely because of the absence of lubrication and, (iii) the active recrystallization processes and especially the nucleation one which can bring new texture components. In the present case, it was not possible to separate the effects of these three items, which would need complex simulations to go a little bit further. However, the expected significant change in the crystallographic texture would be mainly attributed to discontinuous recrystallization.

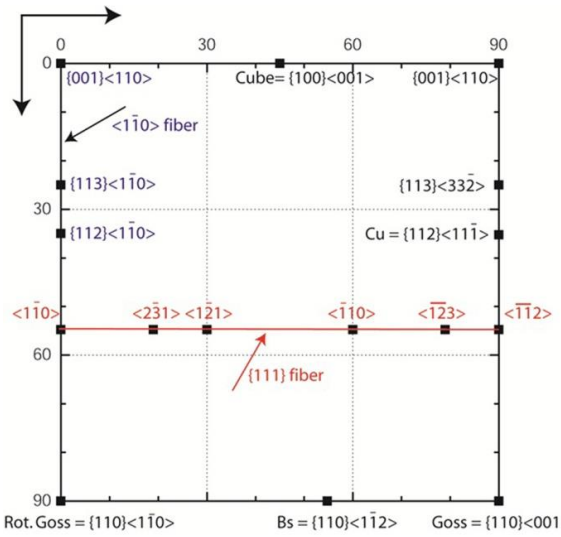

Fig. 1. Main principal texture components for (bcc) and (fcc) metals after rolling or annealing in the $\varphi_2 = 45°$section of the Euler space.

4. Results and discussion

4.1. Effect of hot forging on the microstructure and crystallographic texture evolution

Figs.2a and 2b show the crystal orientation maps of both the austenite and the ferrite phases at the as received state of the material. Both phases exhibit elongated morphologies according to the prior rolling direction of the sheet with an average grain width of about 10µm. The two phases present some morphological differences indicating that they acted differently during the thermomechanical history of the material. Austenite grains (Fig.2a) contain few annealing twins and appear more fragmented than ferrite ones due to their partial recrystallized state. Ferrite grains (Fig. 2b) are still elongated in the rolling direction indicating the occurrence of only recovery during the fabrication process of the sheet, sufficient though to eliminate almost all defects, as deduced from the characterization of the GAM parameter presented below. This difference in behavior of the two phases can be attributed to the difference in the SFE energy of the two phases, but also to the difference in stored energy (stored during the deformation step) that is indeed higher in austenite than in ferrite [29, 30]. Fig. 3 shows X-ray diffractograms obtained after 4 hot forging passes. The as received state is characterized by the presence of only austenite and ferrite peaks. The patterns corresponding to hot forging at 850 °C and 950 °C contain some σ phase peaks. This phase precipitates within the δ ferrite through the diffusion of chromium and molybdenum elements known as σ forming elements [31]. Table 2 displays the various microstructural parameters obtained from X-ray data analysis through a Rietveld refinement analysis conducted using the MAUD software [32]. It is observed that hot forging at 850 and 950 °C results in a significant decrease in the ferrite volume fraction as a consequence of the σ phase formation (see EBSD maps below). Increasing the deformation temperature from 1050 °C up to 1250 C° favors the $\gamma \rightarrow \delta$ phase transformation leading to an increase of the δ ferrite volume fraction. The crystallite sizes for both austenite and ferrite phases are strongly modified by hot forging, compared to the as received state. The largest crystallite sizes for ferrite and austenite were obtained after hot forging at 1150°C and 1250 °C respectively. It is also observed in Table 2 that both ferrite and austenite lattice parameters fluctuate due to internal distortions induced by the hot forging process. It should be noted that the lattice parameters calculated here for ferrite, austenite and σ phase are consistent with those existing in the literature [33]. Additionally, the temperatures at which σ phase

formation is observed during hot forging are the same as the ones identified for σ phase formation during annealing after welding [34].

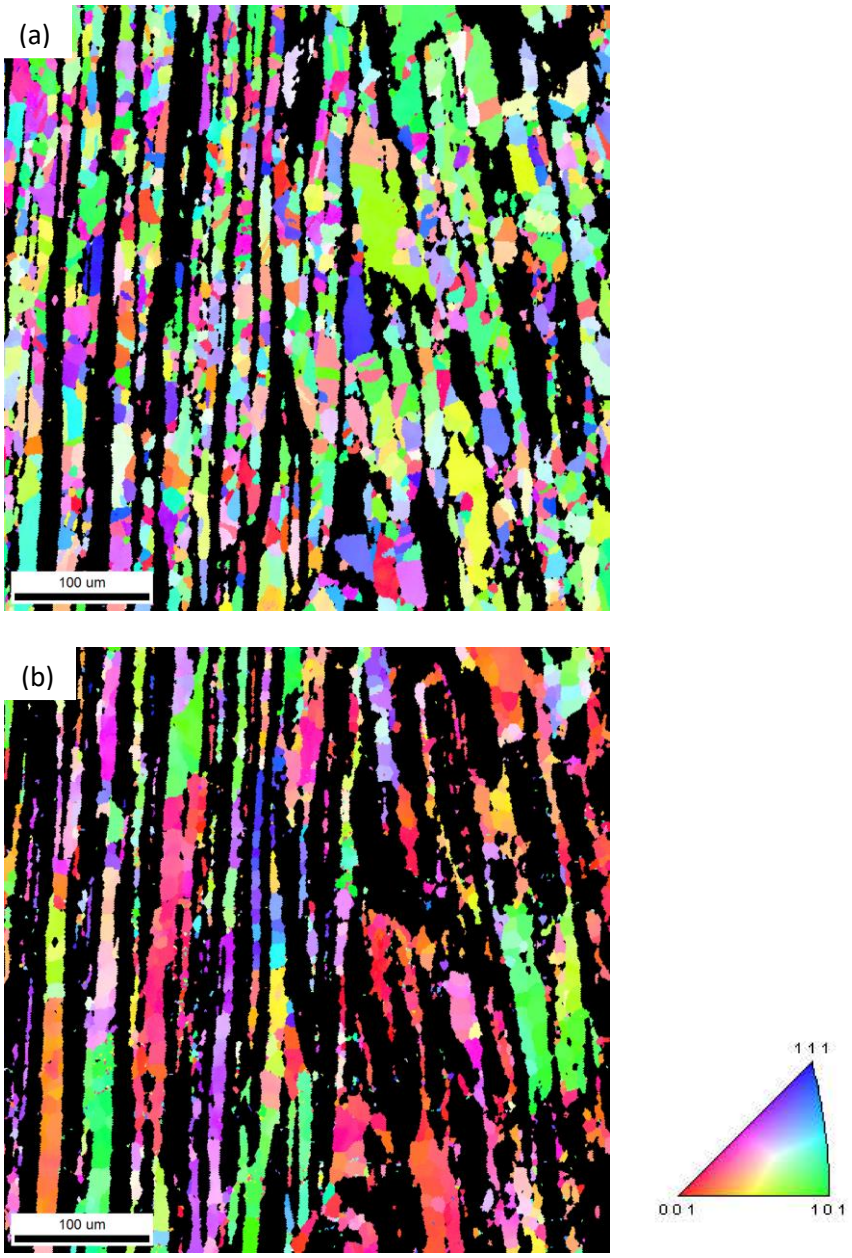

Fig. 2. EBSD orientation maps measured at the as received state, a) austenite, b) ferrite.

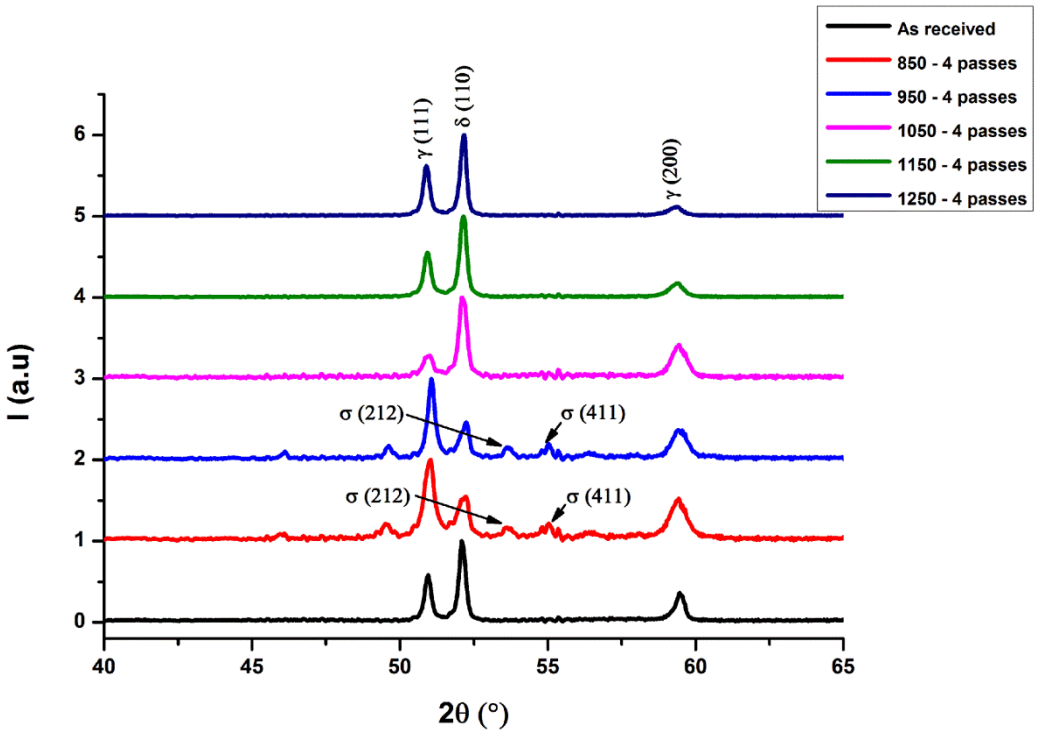

Fig. 3. X-ray diffractogrammes obtained after 4 passes hot forging at different temperatures.

Table 2. Microstructural features extracted from the Rietveld analysis of the X-ray Diffraction data.

		As received	850°C 4 passes	950°C 4 passes	1050°C 4 passes	1150°C 4 passes	1250°C 4 passes
Austenite	Lattice parameter (Å)	3.6059	3.6070	3.6205	3.6078	3.6139	3.6039
	Coherent domain size (Å)	875.83	503.67	420	948.4	840.3	1288.79
	Phase volume fraction (%)	48.32	55.30	49.14	48.7	42.8	34.9
Ferrite	Lattice parameter (Å)	2.8829	2.882	2.8937	2.8803	2.886	2.878
	Coherent domain size (Å)	1321.38	523.68	214	1257.4	2788	1497.93
	Phase volume fraction (%)	51.68	19.79	24.52	51.3	57.2	65.1
σ phase	Lattice parameter a (Å)	//	8.815	8.8596	//	//	//
	Lattice parameter c (Å)	//	4.596	4.617	//	//	//
	Coherent domain size (Å)	//	358.805	//	//	//	//
	Phase volume fraction (%)	//	24.92	26.34	//	//	//

A low magnification image of the 2205 DSS hot forged at 850 C° (i.e. the optimal temperature for σ phase precipitation) for four passes is presented in Fig. 4a. It reveals the presence of many cracks within the surface of the sample. The SEM micrograph presented in Fig. 4b shows the presence of precipitates at the δ/γ interfaces as well as within the δ ferrite grains, which definitely play a role in the crack initiation. The EDS analysis of these precipitates confirmed their correspondence to the well-known σ phase. The chemical composition of the σ phase obtained here (% Cr = 29, % Mo = 9.03, % Ni = 4.03, % Mn = 1.41, % Si = 0.99) is in good agreement with other results published elsewhere [31]. The mechanism of the σ phase formation, its kinetics and its effect on the mechanical behavior of DSS were previously investigated in other papers [31, 35].

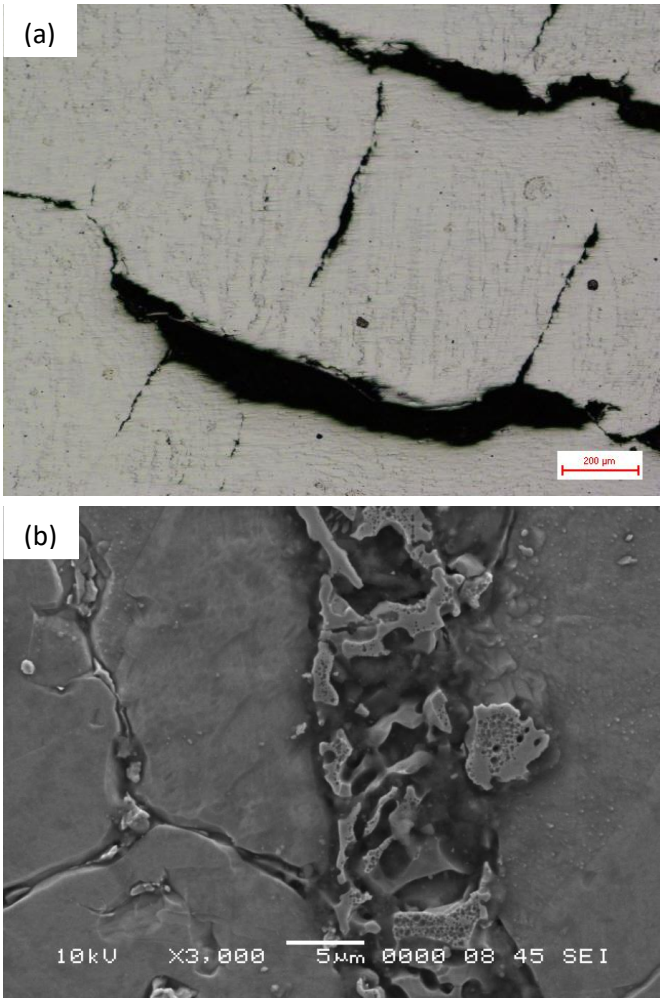

Fig. 4. (a) Optical macrograph of the specimen hot forged at 850°C for 4-passes, (b) SEM micrograph showing the σ phase precipitation after 4-passes hot forging at 850°C.

Fig 5(a-i) shows the EBSD orientation maps obtained after hot forging at 4 different temperatures and Table 3 gathers the quantitative data concerning the grain boundaries extracted from these maps (percentages of LAGBs, HAGBs, average GAM and area occupied by grains associated with a GAM value less than 1°). The common remark is that the initial elongated morphology observed in Fig. 2 is strongly affected by the hot forging process: the morphology, average grain size, degree of fragmentation and orientations evolve indeed strongly during the whole process. This is due to both the effect of simultaneously deformation and recrystallization and the gradual evolution of the percentage of the two phases with the increase of forging temperature (see Table 2).

The morphology and microstructural characteristics of the ferrite and austenite phases present at 850°C (Figs. 5a-c) differ from those obtained at higher temperatures (above 1050°C). This is due to two reasons: (a) the 1h pre-heating time before hot forging leads to significant grain growth, mainly in austenite, since there no transformation occurred in this phase at that temperature, (b), the presence of an additional hard σ phase particles strongly affects the deformation of the softer austenite and ferrite phases during hot forging, which contributes to the strong increase of the LAGB percentage and subsequent drop of the HAGB percentage in that case. Due to the relatively small amount of σ phase and its more brittle character, the GB percentages are less significant in this phase.

A large re-increase of the HAGBs percentage in both austenite and ferrite phases is observed at 1050 °C, compared to 850°C. In the austenite phase (Fig. 5d), the grains undergo significant fragmentation and evolve towards a cellular morphology. This is accompanied by slight changes of the orientation colors, indicating that the processes of DDRX (or PSRX) did not take place. It can thus be assumed that only CDRX has occurred in this case. The hot forging process has also strongly affected the ferrite phase morphology. The rapid diffusion kinetics within ferrite and its high stacking fault energy compared to austenite facilitates the rearrangement and annihilation of dislocations. This favors in turn the modification of the sub-boundaries formed during straining and leads to the formation of polygonal ferrite grains as shown in (Fig. 5e). Thus, DRV or CDRX can be adopted as softening mechanisms acting

during hot forging within the ferrite phase. This is accompanied by an important texture evolution in this phase, as illustrated by the EBSD orientation maps given in Fig 5e, due to grain re-orientation during straining (plane strain compression indeed produces an increase of {111} components in bcc materials).

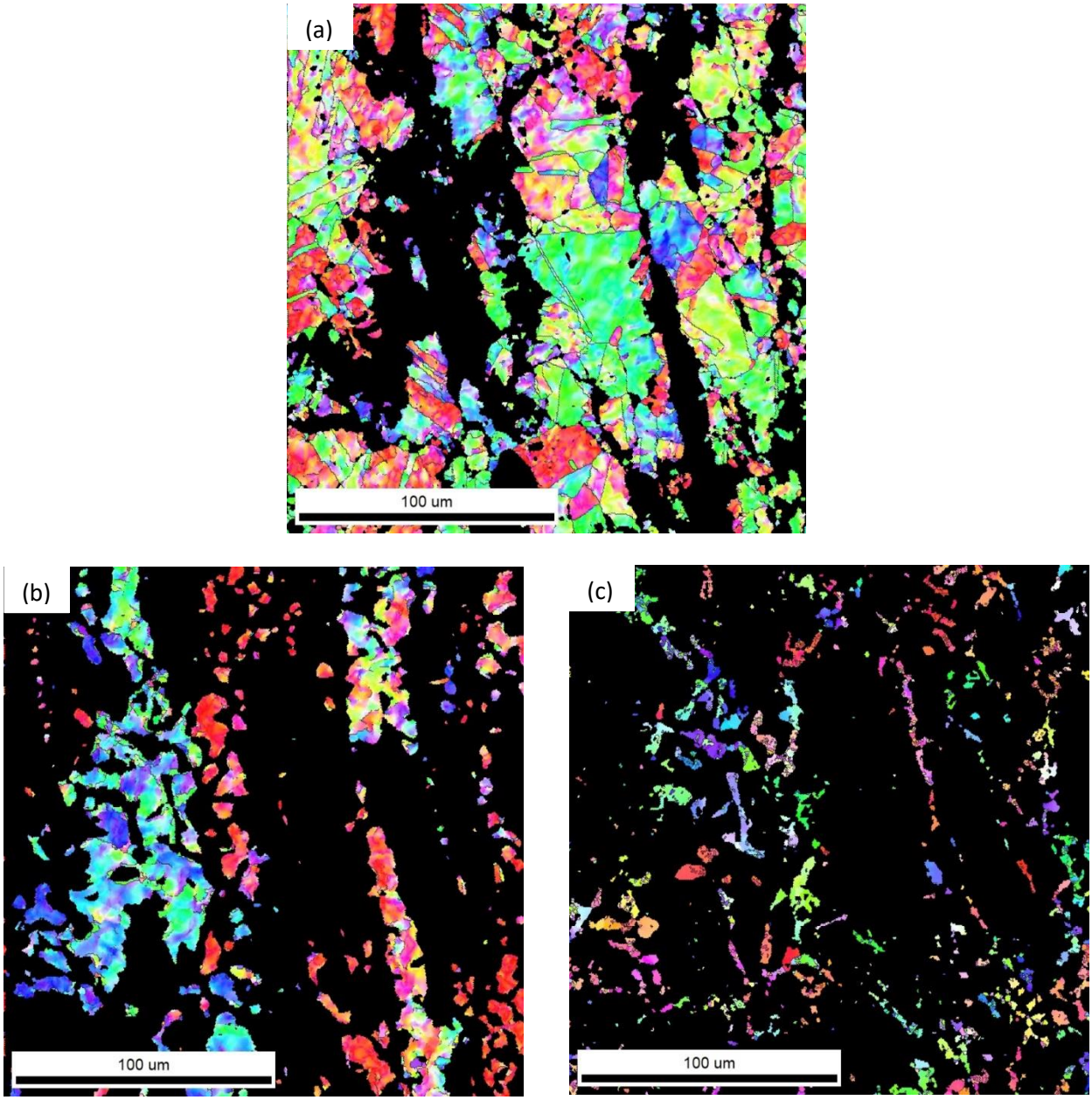

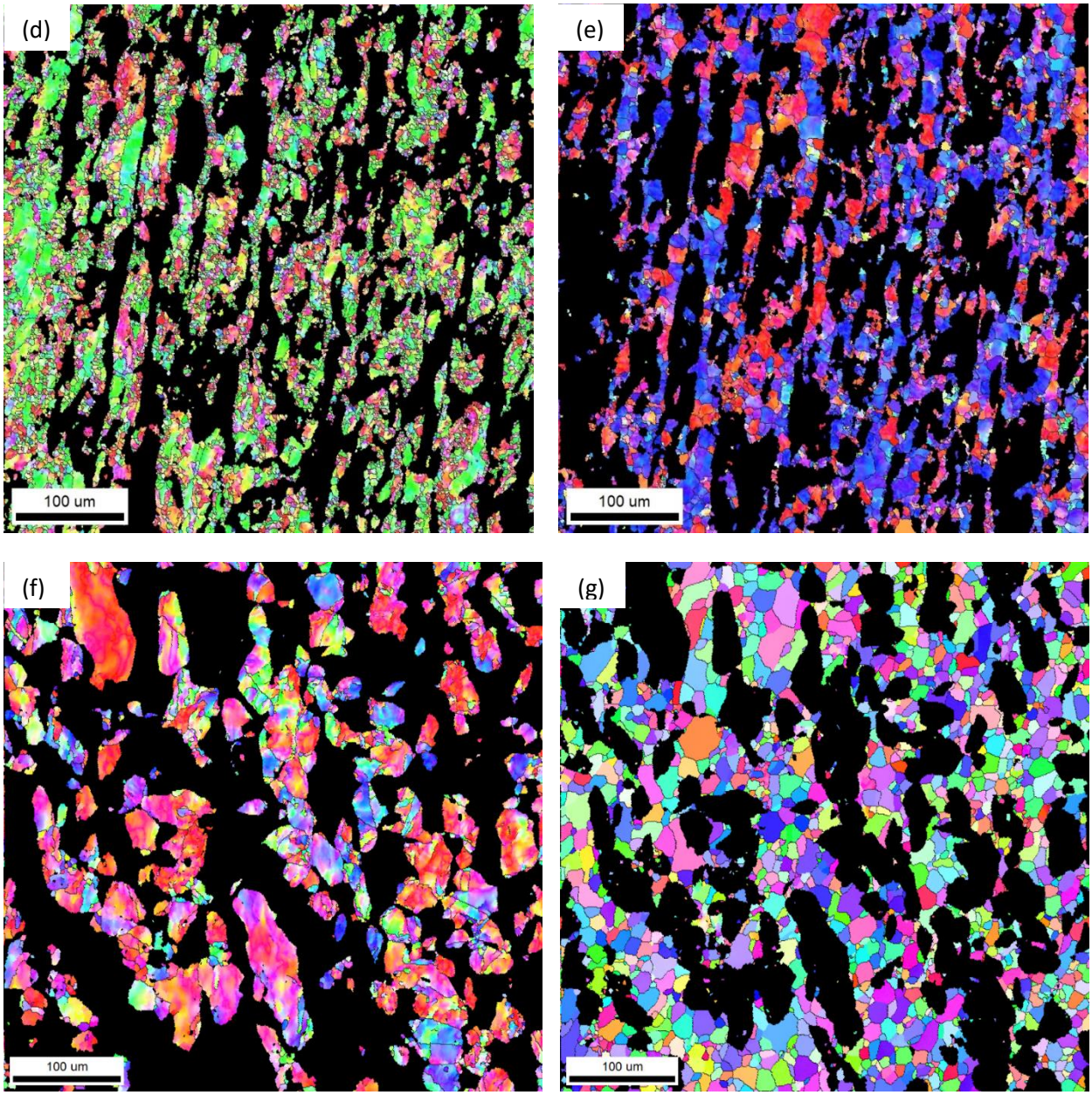
(d)
100 um
(e)
100 um
(f)
100 um
(g)
100 um

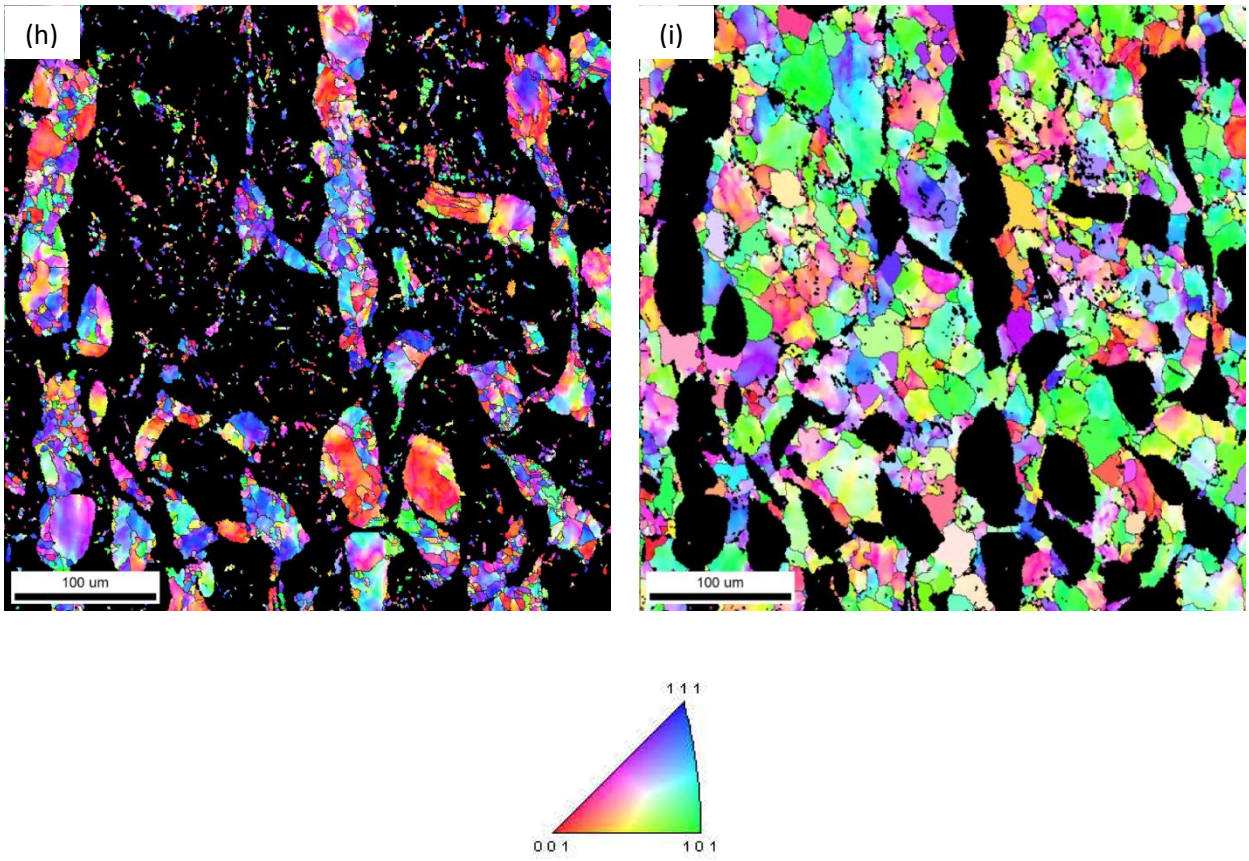

Fig. 5. EBSD orientation maps after 4 passes hot forging for respectively: (a), (b) and (c) austenite, ferrite and sigma phase at 850°C, (d) and (e) austenite and ferrite at 1050°C, (f) and (g) austenite and ferrite at 1150°C, (h) and (i) austenite and ferrite at 1150°C.

Increasing the deformation temperature to 1150 and then to 1250 °C produces further significant microstructural changes. The EBSD orientation map (Fig. 5f) shows that austenite evolves towards a cellular morphology after 4 passes hot forging at 1150 °C. The grains contain some HAGBs that are not completely closed to become new grain boundaries. This suggests that the CDRX process, possibly followed by MDRX, is not complete in austenite after 4 passes hot forging. At the same time, the ferrite undergoes a drastic change (Fig. 5g): the percentage of HAGBs is strongly reduced (from 78% at 1050°C to 23% at 1150°C) and accompanied by a noticeable grain growth. This suggests the activation of either DDRX (and/or PSRX) in this case. All these microstructural changes are accompanied with crystallographic texture changes (see below). A further increase of the deformation

temperature up to 1250 °C (Figs. 5h and 5i) results on the one hand, in the austenite and ferrite grain growth and, on the other hand, in the enhancement of the $\gamma \rightarrow \delta$ phase transformation. As indicated before in Table 2, the austenite volume fraction decreases from 48.7 (at 1050 °C) to 34.9 % (at 1250°C) due to the $\gamma \rightarrow \delta$ phase transformation that occurs through a grain boundary migration process. In the austenite phase (Fig. 5h), the mechanism of CDRX (again possibly followed by MDRX) seems to be once more the main one, whereas in ferrite, the increase of the LAGB percentage suggests that at this very high temperature, we do have DDRX followed by CDRX (and possibly by MDRX) (Fig. 5i). If there is a quite good correlation for the ferrite phase between the coherent domain size (d) measured by X-ray diffraction (Table 2) and the percentage of LAGBs (Table 3) (i.e. the higher the LAGBs percentage is, the lower is (d) value). This is a little bit less true for austenite. This indicates that the process of grain fragmentation during hot forging depends, in a complex way, of the initial state of the material and possible recrystallization mechanisms. Figs. 6 and 7 show the GAM distribution for austenite and ferrite in the investigated DSS. According to Nicolay et al. [22] and Zaho et al. [23], a GAM value below 1° corresponds to recrystallized grains. Nicolay et al [22] and, thanks to the development of a new analysis procedure, distinguished between DRX and PDRX grains. Unfortunately, the present analysis does not allow performing this distinction. As shown in Figs. 6 and 7, both ferrite and austenite at the as received state exhibit a prominent GAM peak below 1°, indicating a total recrystallized state in both phases. Table 3 shows that both ferrite and austenite phases have similar average GAM values equal to 0.79 and 0.76 respectively. After hot forging, the GAM distributions evolve differently in the two phases. In the austenite phase (Fig. 6), a significant dispersion is observed in the GAM distribution for all temperatures, although it is slightly reduced at the highest temperature (Fig. 6).

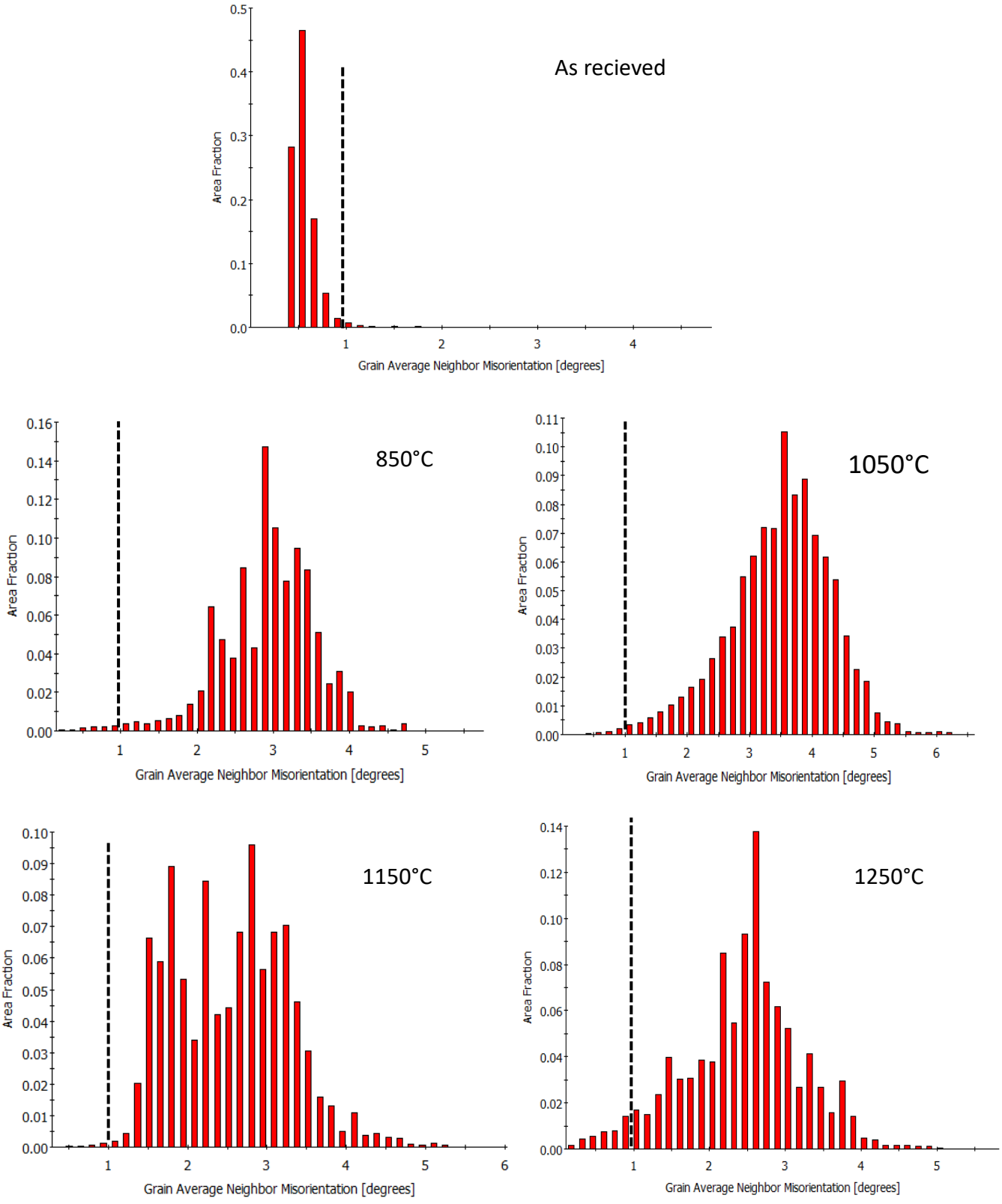

Fig. 6. GAM profiles assessed for the austenite phase in the as received state and after hot forging at various temperatures. The black dashed line indicates the difference between recrystallized from deformed grains.

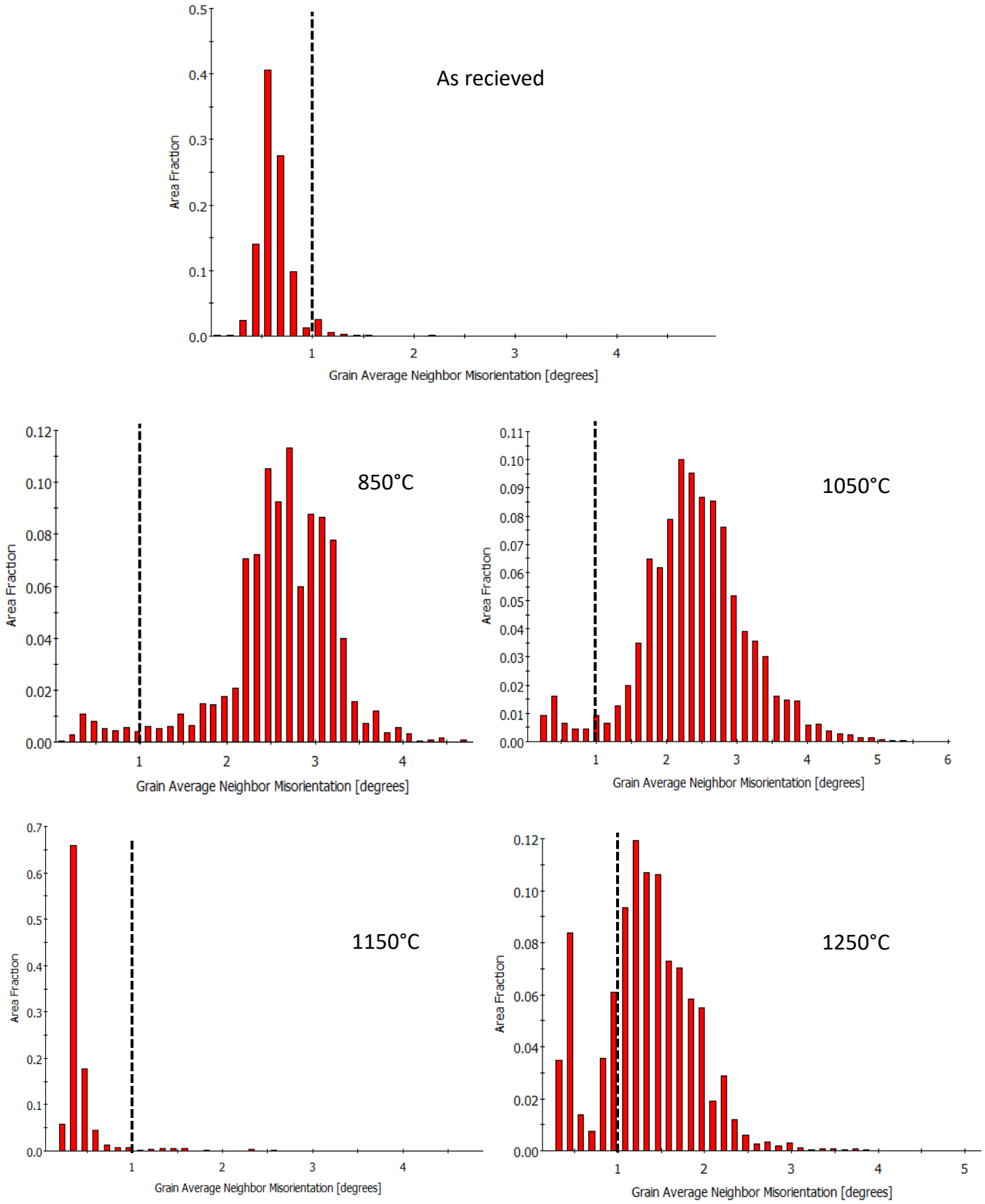

Fig. 7. GAM profiles assessed for the ferrite phase in the as received state and after hot forging at various temperatures. The black dashed line indicates the difference between recrystallized from deformed grains.

The fraction of recrystallized grains is very small (below 1%) at 1050 and 1150°C (see Table 3). In the ferrite phase (Fig. 7), we can say first that all samples comprise a percentage of recrystallized grains (at least 4%, see Table 3), and that the GAM distribution of ferrite presents always less dispersion than that of austenite (especially, the maximum value is always lower in the ferrite phase). Also, it is quite clear that the ferrite is completely recrystallized after forging at 1150°C. All these observations are in good agreement with the mechanisms proposed above: CDRX, very active in the austenite phase produces an increase of the average GAM, whereas DDRX, active in the ferrite phase at 1150°C produces a drastic decrease of the average GAM. Also, the fact that the average GAM is the highest in the ferrite phase deformed at 1050°C is in favor of the sole DRV process at this temperature. As for the possible occurrence of PDRX mechanism, we can say that MDRX is most probably active in all cases, but not PSRX (which needs an incubation time to start), since it would have led to much larger proportions of recrystallized grains and a drastic reduction of the dispersion in the GAM distribution.

Table 3. Fractions (in %) of LAGBs, HAGBs (in %), average GAM values and recrystallized fractions (grains associated with a GAM < 1°), calculated from EBSD data within the main ferrite and austenite phases.

		As received	850 – 4 passes	1050 – 4 passes	1150 – 4 passes	1250 – 4 passes
% LAGBs	Austenite	12.2	88.7	70.2	88.2	77.5
	Ferrite	58.7	91.3	78.4	22.7	75.3
% HAGBs	Austenite	86.8	11.3	29.3	11.7	22.1
	Ferrite	41.3	8.7	21.4	76.6	24.6
Average GAM (°)	Austenite	0.76	2.46	3.31	2.79	2.18
	Ferrite	0.79	2.06	2.51	0.81	1.60
Area fraction (%) associated with GAM < 1°	Austenite	98.7	1.0	0.5	0.7	4.47
	Ferrite	91.1	4.1	4.6	93.5	22.08

It is now important to examine the effect of the hot forging process on the crystallographic texture evolution of the studied DSS. The φ_2 = 45° ODF section of the as received state (Fig. 8a) indicates that austenite crystallographic texture is mainly composed of a major Brass={110}⟨112⟩ (Bs) component with a maximal intensity of 5.5. A weak Goss={110}⟨001⟩ component is also observed. These texture components have been typically observed in austenite in other research works after rolling and annealing [36, 37]. The crystallographic texture of the ferrite phase in the as received state (Fig. 8b) is mainly composed of the rotated Cube = {001}⟨110⟩ component, with some spread along the {001} // ND fibre. It is interesting to note that there exists a marked orientation relationship typical from the $\delta \rightarrow \gamma$ phase transformation, between the main component of each phase. the misorientation between the rotated Cube orientation in the ferrite phase and the Bs orientation in the austenite phase is indeed equal to 45.99° around a [0.2, 0., 0.976] axis, which is very close to the Nishiyama – Wasserman relationship [38, 39].

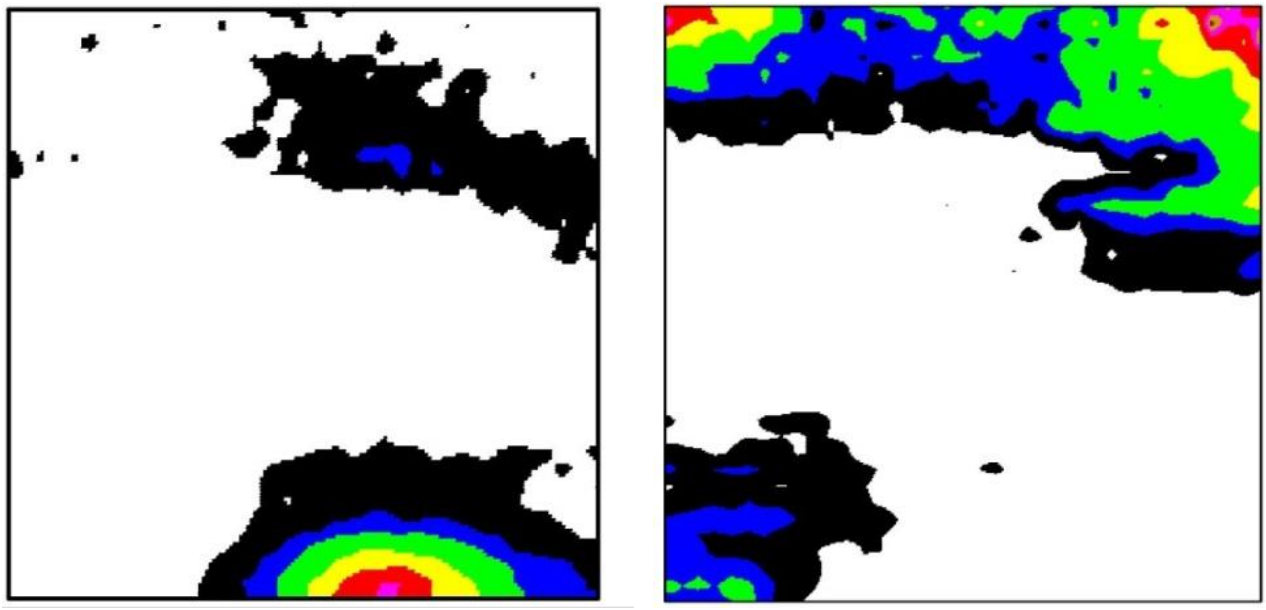

(a) (b)

Fig. 8. ODF (φ2 = 45°sections) measured at the as received state, (a) austenite and (b) ferrite

During hot forging (Figs. 9 and 10), there is a general spreading of the texture components along {hkl} fibres (horizontal lines within the section) in both phases, which can be attributed to the effect of uniaxial compression and of the fragmentation of the grains. In the austenite phase, a strong weakening of its crystallographic texture after hot forging at 850° is observed (Fig 9a). This spreading is consistent with the fragmentation and reorientation of the grains during forging. Hot forging at 1050 °C leads then to the appearance of the rotated Goss={110}⟨110⟩ component (Fig 9b) in addition to the existing weak Bs component. This rotated Goss component is further reduced at 1150°C (Fig 9c), while some new components close to {112}<110> appear. Increasing the deformation temperature to 1250°C produces a strong change of austenite crystallographic texture (Fig 9d): both rotated Goss and Bs components have disappeared and a {111}⟨110⟩ texture component is now observed in the austenite phase, which is quite unusual in this phase.

In the ferrite phase, the rotated Cube component disappears during hot forging at 850 °C and is replaced by a weak texture distributed along several fibres (Fig. 10a). Increasing the forging temperature from 850 °C to 1250 °C (Figs. 10b to 10d) further modifies the crystallographic texture of the material, which becomes composed of a main {001} // ND fibre at 1150°C and a main {113}// ND fibre at 1250°C (fig. 10d). Again the texture found within the ferrite phase at 1250°C is quite unusual, although {113} components are often observed in electrical ferritic steels after recrystallization [40]. This texture is the result of a complex thermomechanical path for which some important details are not known (active deformation systems at high temperature, exact deformation path, degree of recrystallization). In any case, the quite unusual texture components observed at the highest forging temperature could be due to the simultaneously effect of partial DDRX in both phases (there is indeed almost 5% recrystallized grains in the austenite phase at 1250°C, and 22% in the ferrite phase). and possibly, In addition, the presence of an additional 'in-plane' shear component (like in asymmetrical rolling) which, in the extreme case, tend to "invert" the BCC and FCC rolling textures, may explain the presence of some unusual texture compnents [41, 42].

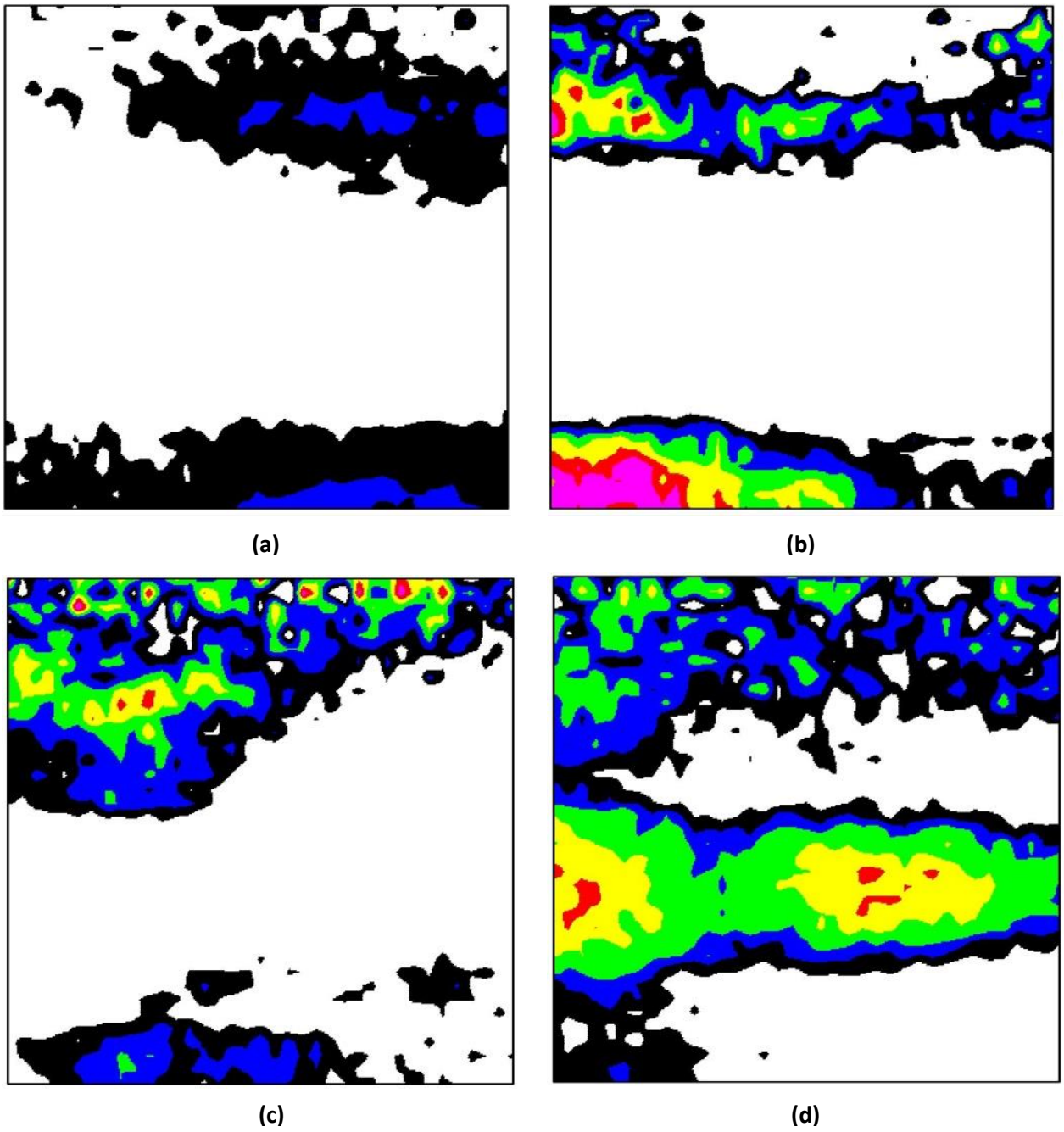

Fig. 9. ODF (φ2 = 45°sections) of austenite after 4 passes hot forging at: (a) 850°C (b) 1050°C (c) 1150°C and (d) 1250°C

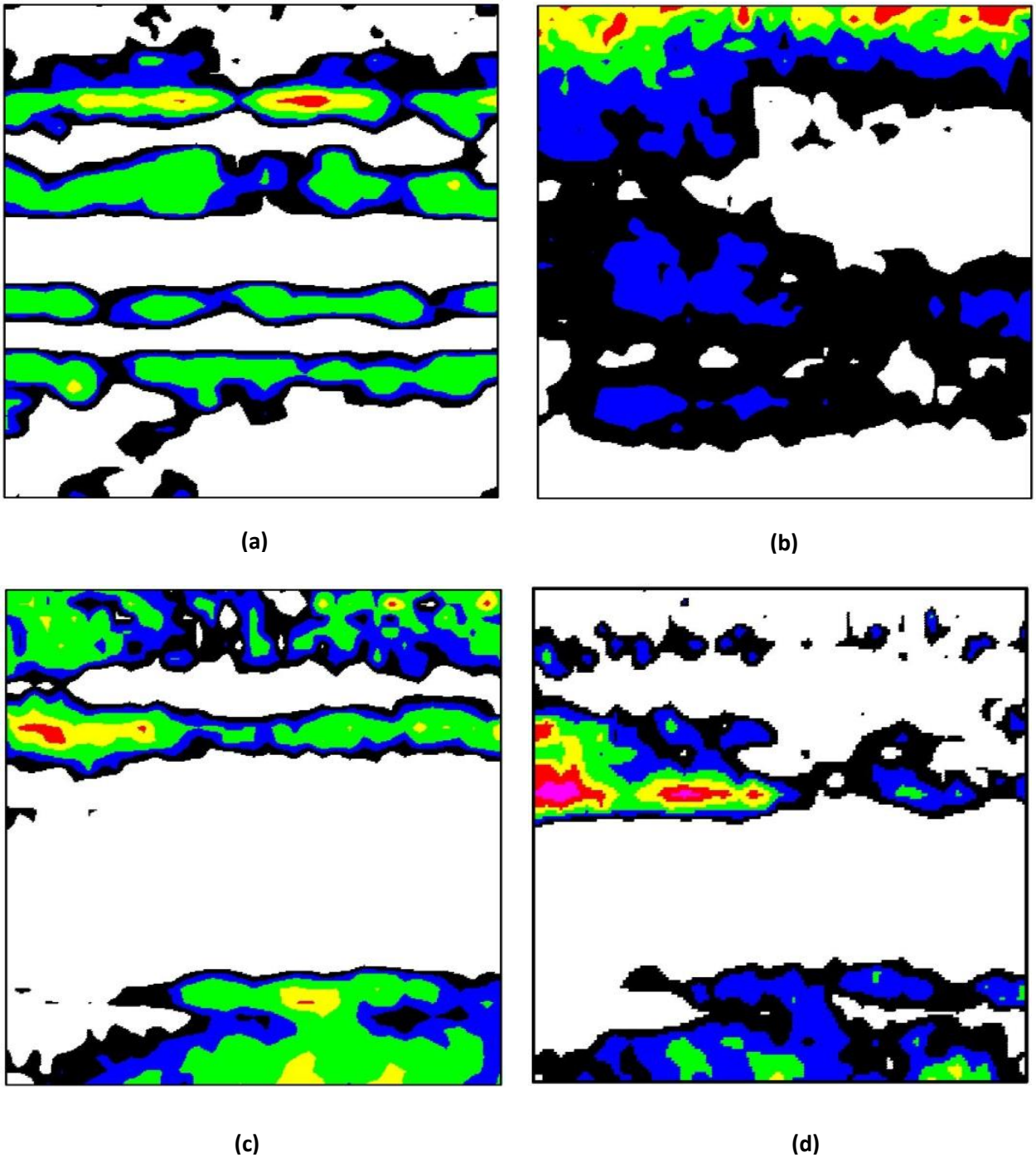

Fig. 10. ODF (φ2 = 45°sections) of ferrite after 4 passes hot forging at: (a) 850°C (b) 1050°C (c) 1150°C and (d) 1250°C

4.2. Investigation of the mechanical behaviour

The true stress-true strain curves of the 2205 DSS hot forged at different temperatures are given in Fig. 11. The mechanical properties determined from this figure for each deformation domain are given in Table 4. It can be noticed that both yield strength σ_e and tensile strength σ_u increase significantly after hot forging at 850°C (compared to the as received state of the material) and then decrease continuously with a further increase of the forging temperature up to 1250°C. At the same time, the fracture stress σ_f drastically decreases after hot forging at 850°C; it increases again for higher forging temperatures, but remains always lower than in the as received state. The yield strain ε_e is hardly modified by the hot forging process whatever the temperature, both maximum strain ε_u and fracture strain ε_f decrease drastically after hot forging at 850°C in comparison to the as received state. As already mentioned previously, the precipitation of the σ phase (described above in Fig. 3) occurs at this temperature, which seriously limits the dislocation movement at the vicinity of the grain boundaries. The σ phase particles destroy the microstructural continuity at the δ/γ interface [43] and form an inescapable barrier that prevents the dislocation mobility at the δ/γ interfaces during deformation. Hence, the dislocations ensuring the plastic straining of austenite and ferrite are blocked at the γ/σ and δ/σ interfaces and resist to the plastic deformation process. Consequently, the material's damage increased at these interfaces due to the increase of the stress and strain levels and the presence of hard particles that resulted in the drastic loss of ductility (illustrated in Table 4) and the cracking phenomenon illustrated before in Fig. 3a. The occurrence of the plastic flow after hot forging at 850 and 950 °C requires higher strength values that resulted in the increase of the material's yield strength. Hot forging of the 2205 DSS at temperatures ranging from 1050 to 1250 °C resulted in improved mechanical properties compared to those obtained at 850 and 950°C due to, on the one hand, the absence of the σ phase and, on the other hand, to dynamic recovery and recrystallization occurring at these temperatures. The best compromise between ductility and resistance to plastic deformation is evaluated through the calculated values of the product $\sigma_u . \varepsilon_u$ (see table 4). In that sense, once the negative influence of the σ phase is suppressed, all 3 higher temperatures are more or less equivalent, since this parameter varies between 2.1 and 2.2.

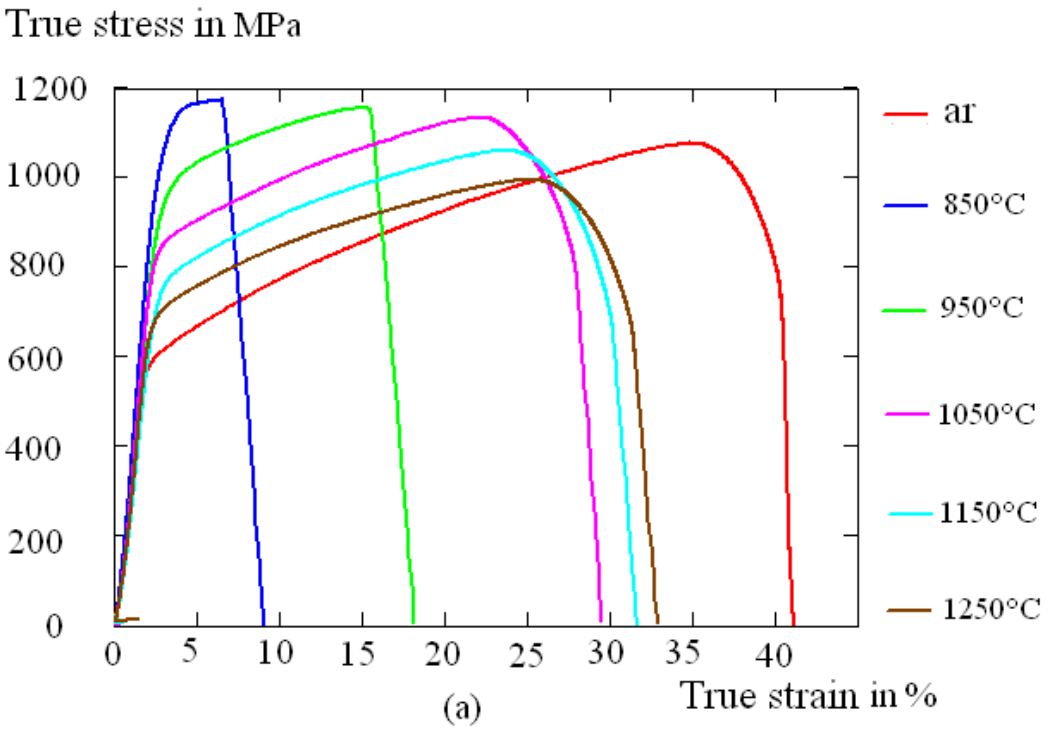

Fig 11. True stress-true strain curves after different forging temperatures.

Table 4: Mechanical properties of the hot forged 2205 DSS determined from Fig. 11.

Forging temperature	As received	850°C	950°C	1050°C	1150°C	1250°C
Yield strength σ_e in Mpa	495.82	807.48	766.17	687.68	604.91	593.86
Yield strain ε_e in %	1.34	1.76	1.83	1.63	1.79	1.61
Tensile strength σ_u	1076.7	1173.7	1154.4	1133.9	1059.3	994.31
Maximum strain ε_u in %	31.98	3.73	11.41	19	20	22.09
Empirical parameter $\sigma_u . \varepsilon_u$	3.4	0.44	1.3	2.15	2.11	2.2
Fracture stress σ_f	643.22	150.83	620.73	781.34	641.18	574.49
Fracture strain ε_f	0.3864	0.0814	0.1495	0.2583	0.2805	0.2974

Fig. 12a shows typical load-displacement (P-h) curves conducted in ferrite, austenite and sigma phase. The data collected from Fig. 12a shows that the elastic modulus values of austenite are slightly higher than those of ferrite ($335 \pm 4\ GPa\ and\ 330 \pm 2\ GPa$, respectively), while the nanohardness of ferrite is lower. This is in good agreement with the results found by Kheradmand et al. [45]. The difference in microscopic residual stresses between ferrite and austenite grains, with different thermal expansion coefficients, induced after quenching from an elevated temperature, allows to nitrogen element to play a crucial role in stabilizing austenite and acts as a planar slip promoter that enhances the strength of austenite [46-48]. As expected, the indentation depth of sigma phase (red line in fig. 12a) is less deep than that of austenite and ferrite phases. This indicates that the nanohardness and young modulus of sigma phase are the highest (8.2 ± 0.6 GPa and 342 ± 2 GPa, respectively) because of the elements nature (Cr-Mo), as well as the complexity of its crystalline structure [49].

Fig. 12b shows P-h curves of ferrite for samples subjected to 4 passes hot forging at different temperatures. It is observed that the lower hardness and elastic modulus values are recorded in the as-received condition with $3.2 \pm 0.3\ \ GPa$ and $274 \pm 4\ GPa,$ respectively. Hot forging at 850°C increased the hardness and the Young's modulus of the steel ($7.4 \pm 0.2\ GPa$ and $329 \pm 3\ GPa$ respectively). A further increase in forging temperature up to 1250 °C resulted in a decrease of these characteristics. The observed increase in the mechanical properties is attributed to the work hardening that was induced by the dislocation nucleation phenomena [44]. In general, after the plastic deformation, in that case hot-forging, the change of bonding force between atoms causes a decrease in elastic modulus. The main reasons to that are: impurity, secondary phases, grain orientations, dislocations and so on [50]. In the present work, the high elastic modulus of sigma phase can explain the increase in elastic modulus after 4-passes hot-forging at 850°C and 950°C. However, after hot forging at high temperatures (1050°C-1250°C), the important texture evolution observed in ferrite caused by the CRDX discussed in Section 4.1, resulted in a softened microstructure due to the low dislocation density with relatively low H_{IT} and elastic modulus (see Table 5).

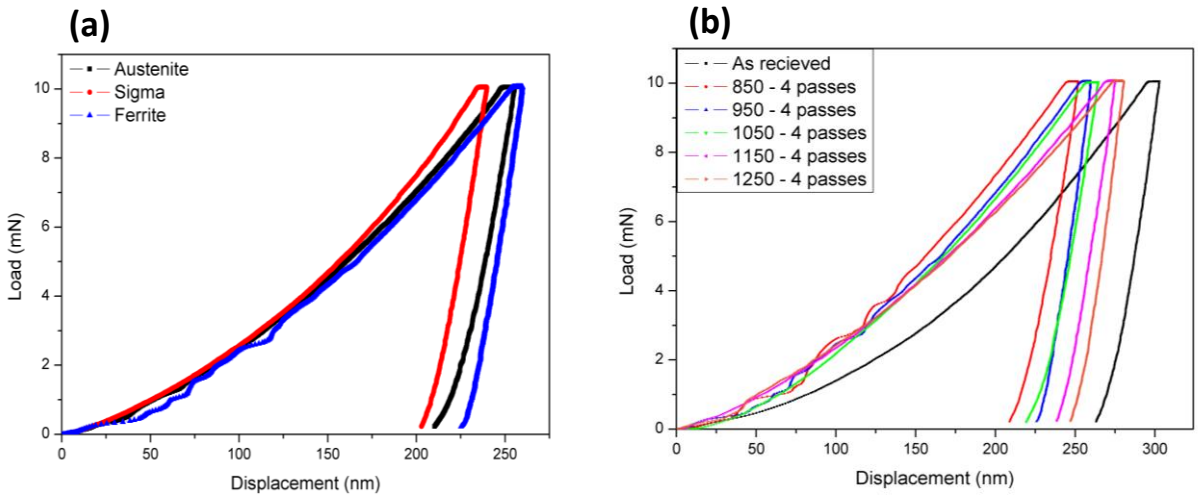

Fig. 12: Nanoindentation load-displacement curves of samples obtained after 4 passes hot forging : (a) – P-h curves of different phases (ferrite, austenite and sigma phase) at 850° (b) – Conducted in ferrite phase of samples at different temperatures.

A zoom view of loading segment of P-h curves (Fig 12b) shown in Fig. 13 (a-c), exhibits a significant difference during loading process of the as-received, 850°C and 1250°C 4-passes hot forged samples. A distinguished sudden displacement, known as pop-in, is observed in the initial part of P-h curves in the as-received sample and barley detected after 4-passes hot forged at 850°C sample. This phenomenon disappears for further hot forging temperature. This is attributed to the elastic straining by nanoindentation test that can be fitted using the Hertzian elastic contact solution according to Eq. (1), where the tip shape is considered spherical at shallow depths [51] as illustrated in Fig.13a and 13b.

$$P = \frac{4}{3} E_r \sqrt{Ri}\, h^{3/2} \qquad (1).$$

Where: P is the applied load, E_r is the reduced Young's modulus, R_i is the curvature of the indenter (500 nm) and h is the displacement into surface.

It was assumed that the first pop-in (Fig. 13a) is generally related to the drastic homogeneous dislocation nucleation or dislocation source activation [44] where the ferrite phase starts to deform plastically in the very early stage of the indentation process (250-300 μN). Taking into account the large tip radius and irregularity in tip geometry, the critical shear stress value for the homogeneous dislocation nucleation

cannot be presented with absolute precision. Nevertheless, the maximum shear stress (τ_{max}) underneath the indenter calculated in the as-received condition using Eq. (2),

$$\tau_{max} = 0.18\,[\frac{6}{\pi^3}\frac{P\,{E_r}^2}{R^2}]^{1/3} \qquad (2).$$

is found to be (4.2 GPa) in the same order of the theoretical strength of the free-defect iron crystal ($\frac{1}{25} < \tau < \frac{1}{15}$) where the shear modulus of ferrite is approximately 83 GPa [51]. Suggesting that the pop-in is occurred in free-defect area.

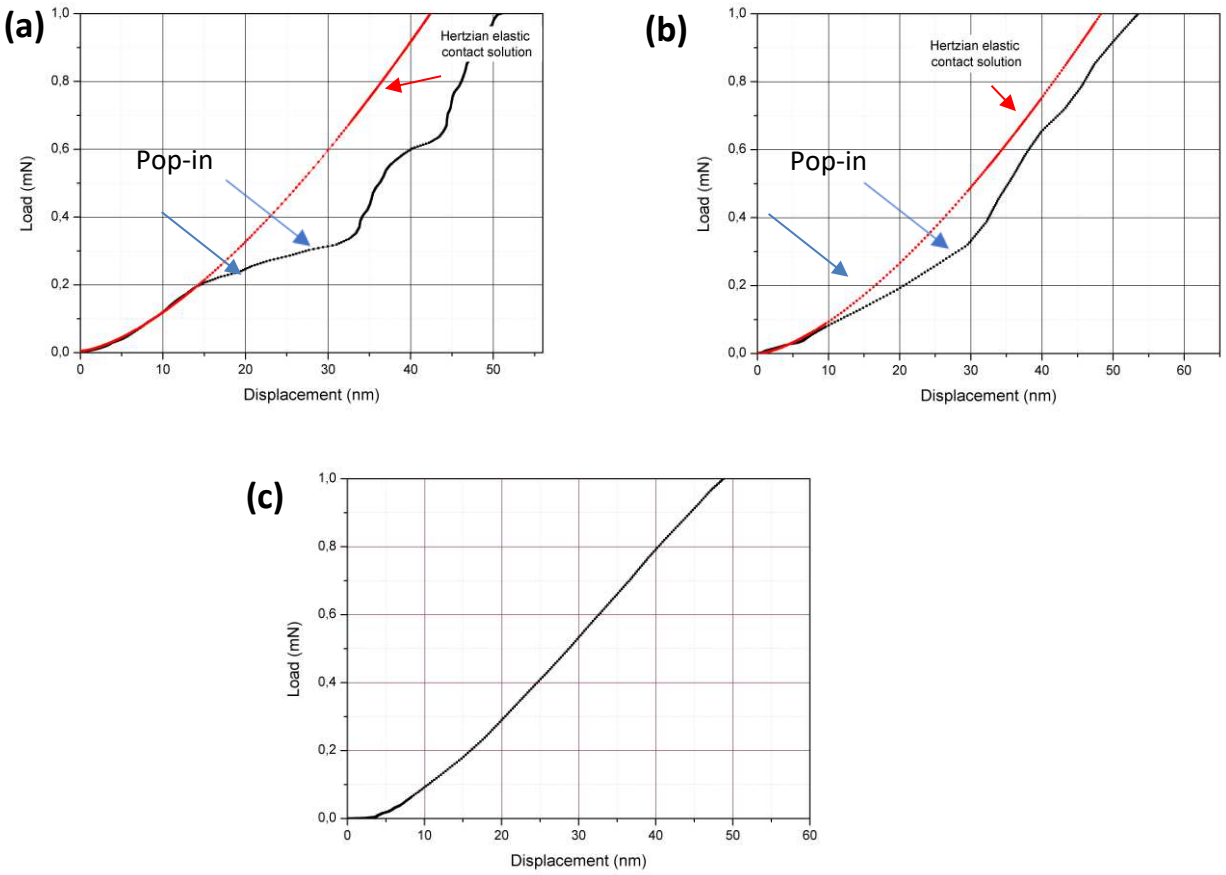

Fig. 13: Zoom view of loading segment of P-h curves of Fig. 12b including Hertzian elastic contact solution for (a): as-received state, (b) and (c): those obtained after 4 passes hot forging at 850°C 1250°C respectively.

Hot forging at 850°C resulted in the lack of pronounced pop-in effect (Fig. 13b) that is explained by the movement and multiplication of unlocked existent dislocations by high shear stress. It is clear that the dislocation density in the deformed material play a key role in the pop-in occurrence. The high dislocation density exists under the indenter tip in the pre-strained material i., e. 4-passes hot forged sample at 1250°C, promotes the dislocation activation and multiplication under a lower shear stress rather than the nucleation of new dislocation at very high stresses [52, 53]. Consequently, the disappearance of pop-in indicates that elastic-plastic deformation occure right at the beginning of the indentation experiment in highly deformed material (Fig. 13c). Therefore, based on nanoindentation tests, hot forging at 850°C and 950°C induced work hardening of ferrite phase by dislocation nucleation phenomena. The presence of sigma phase (with high H_{IT} and E_{IT}) at these temperatures is the origin of the high macro-mechanical properties given in Table 4. On the other side, the softening microstructure of ferrite obtained after hot forging at high temperature (1050°C-1250°C) as a result of CRDX, caused a decrease in hardness and elastic modulus that comes down to reduce the global mechanical properties already issued from uniaxial tensile test.

5. Conclusions

In this work, hot forging of a 2205 DSS performed in the temperature range of 850 to 1250 °C was investigated. The main conclusions of the conducted microstructural and mechanical investigations are given as follows:

- Hot forging of the 2205 DSS at temperatures below 950°C resulted in a sharp cracking phenomenon due to the combined effect of both σ phase precipitation and severe plastic strain that affected drastically its mechanical properties.
- The active recrystallization mechanisms during hot forging have been identified from the analysis of LAGBs and HAGBs percentages and GAM distributions in both phases. In the ferrite phase, DRV was found to be principally active below 1050°. It was then followed by CDRX above this temperature, massively supplemented by DDRX at higher temperatures and especially at 1150°C. In the austenite phase, CDRX was observed at all forging temperatures. From the measured recrystallized fraction and the appearance of new texture components which could not be explained

otherwise. Partial DDRX was also supposed to be active at the highest temperature in austenite.

- A significant texture evolution was observed at all temperatures, under the simultaneous action of re-orientation due to plastic strain, recrystallization and transformation processes. The final textures presented a fiber-like character, mainly due to the uniaxial character of the compression process.
- The observed crystallographic textures after 1250°C in both phases were found to be quite unusual. A strong additional in plane shear component (due to friction effect), supplemented by partial DDRX, could be responsible for this evolution.

- The forging temperature variation strongly affected the mechanical behavior of the investigated material. While a sharp increase of strength and drastic loss of plasticity were recorded after hot forging at 850°C, a progressive gain of plasticity is noticed when increasing the forging temperature from 1050 °C to 1250°C.
- The microstructural and mechanical investigations conducted in this work allow us to conclude that the best combination of microstructure and mechanical properties of the hot forged 2205 DSS was obtained after hot forging at 1050°C, which precisely corresponds to the temperature range for which DDRX becomes massively active.

Acknowledgments. The financial support of the research Center in Industrial Technologies CRTI is gratefully acknowledged. The French ANR (*Agence Nationale de la Recherche*) and CGI (*Commissariat à l'Investissement d''Avenir*) are gratefully acknowledged for their financial support of this work through grants **ANR-10-LABX-0096** and **ANR-18-IDEX-0001**.

References

1. Jorge AM, Reis GS, Balancin O (2011) Influence of the microstructure on the plastic behaviour of duplex stainless steels. Materials Science and Engineering A 528:2259–2264. https://doi.org/10.1016/j.msea.2010.11.087

2. Martinho, R.P., Silva, F.J.G., Martins, C. *et al.* Comparative study of PVD and CVD cutting tools performance in milling of duplex stainless steel. *Int J Adv Manuf Technol* 102, 2423–2439 (2019). https://doi.org/10.1007/s00170-019-03351-8

3. Ren X, Chen X, Xiong Z (2018) Characterization and analysis of diffusion bonding process in a Cr25Ni7Mo4MnSi duplex stainless steel. Journal of Manufacturing Processes 34:603–613. https://doi.org/10.1016/j.jmapro.2018.07.005

4. Cizek P, Wynne BP (1997) A mechanism of ferrite softening in a duplex stainless steel deformed in hot torsion. Materials Science and Engineering A 230:88–94. https://doi.org/10.1016/s0921-5093(97)00087-7

5. Liu Y, Yan H, Wang X, Yan M (2013) Effect of hot deformation mode on the microstructure evolution of lean duplex stainless steel 2101. Materials Science and Engineering A 575:41–47. https://doi.org/10.1016/j.msea.2013.03.036

6. Iza-Mendia A, Pinol-Juez A, Urcola JJ, Gutierrez I (1998) Microstructural and Mechanical Behavior of a Duplex Stainless Steel under Hot Working Conditions. Metallurgical and Materials Transactions A: Physical Metallurgy and Materials Science 29:2975–2986. https://doi.org/10.1007/s11661-998-0205-z

7. Mehtonen S V., Palmiere EJ, Misra RDK, et al (2014) Dynamic restoration mechanisms in a Ti-Nb stabilized ferritic stainless steel during hot deformation. Materials Science and Engineering A 601:7–19. https://doi.org/10.1016/j.msea.2014.02.039

8. Mehtonen S V., Karjalainen LP, Porter DA (2013) Hot deformation behavior and microstructure evolution of a stabilized high-Cr ferritic stainless steel. Materials Science and Engineering A 571:1–12. https://doi.org/10.1016/j.msea.2013.01.077

9. Satheesh Kumar SS, Vasanth M, Singh V, et al (2017) An investigation of microstructural evolution in 304L austenitic stainless steel warm deformed by cyclic channel die compression. Journal of Alloys and Compounds 699:1036–1048. https://doi.org/10.1016/j.jallcom.2016.12.321

10. Nezakat M, Akhiani H, Hoseini M, Szpunar J (2014) Effect of thermo-mechanical processing on texture evolution in austenitic stainless steel 316L. Materials Characterization 98:10–17. https://doi.org/10.1016/j.matchar.2014.10.006

11. Yanushkevich Z, Lugovskaya A, Belyakov A, Kaibyshev R (2016) Deformation microstructures and tensile properties of an austenitic stainless steel subjected to multiple warm rolling. Materials Science and Engineering A 667:279–285. https://doi.org/10.1016/j.msea.2016.05.008

12. Ryan ND, McQueen HJ (1990) Flow stress, dynamic restoration, strain hardening and ductility in hot working of 316 steel. Journal of Materials Processing Tech 21:177–199. https://doi.org/10.1016/0924-0136(90)90005-F

13. Balancin O, Hoffmann WAM, Jonas JJ (2000) Influence of microstructure on the flow behavior of duplex stainless steels at high temperatures. Metallurgical and Materials Transactions A: Physical Metallurgy and Materials Science 31:1353–1364. https://doi.org/10.1007/s11661-000-0254-4

14. Duprez L, De Cooman BC, Akdut N (2002) Flow stress and ductility of duplex stainless steel during high-temperature torsion deformation. Metallurgical and Materials Transactions A: Physical Metallurgy and Materials Science 33:1931–1938. https://doi.org/10.1007/s11661-002-0026-4

15. Dehghan-Manshadi A, Hodgson PD (2008) Effect of δ-ferrite co-existence on hot deformation and recrystallization of austenite. Journal of Materials Science 43:6272–6277. https://doi.org/10.1007/s10853-008-2907-4

16. Fan GW, Liu J, Han PD, Qiao GJ (2009) Hot ductility and microstructure in casted 2205 duplex stainless steels. Materials Science and Engineering A 515:108–112. https://doi.org/10.1016/j.msea.2009.02.022

17. Ul-Haq, A; Weiland, H; Bunge H. (1994) Textures and microstructures in duplex stianless steel. Materials Science and Technology 10: (4):289-298 DOI: 10.1179/026708394790163906.

18. Padilha AF, Randle V, Machado IF (1999) Microstructure and microtexture changes during solution nitriding to produce austenitic case on ferritic-austenitic duplex stainless steel. Materials Science and Technology 15:1015–1018. https://doi.org/10.1179/026708399101506869

19. Cizek P, Wynne BP, Rainforth WM (2006) EBSD investigation of the microstructure and texture characteristics of hot deformed duplex stainless steel. Journal of Microscopy 222:85–96. https://doi.org/10.1111/j.1365-2818.2006.01576.x

20. Patra S, Ghosh A, Singhal LK, et al (2017) Hot Deformation Behavior of As-Cast 2101 Grade Lean Duplex Stainless Steel and the Associated Changes in Microstructure and Crystallographic Texture. Metallurgical and Materials Transactions A: Physical Metallurgy and Materials Science 48:294–313. https://doi.org/10.1007/s11661-016-3759-1

21. Moura AN de, Favarato LNO, Itman Filho A, et al (2017) Study of the recrystallization and crystallographic texture evolution during final annealing of UNS S32304 Lean Duplex stainless steel. Materials Characterization 130:39–49. https://doi.org/10.1016/j.matchar.2017.05.025

22. Nicolaÿ A, Franchet JM, Cormier J, et al (2019) Discrimination of dynamically and post-dynamically recrystallized grains based on EBSD data: application to Inconel 718. Journal of Microscopy 273:135–147. https://doi.org/10.1111/jmi.12769

23. Zhao J, Wang K, Huang K, Liu G (2019) Recrystallization behavior during hot tensile deformation of TA15 titanium alloy sheet with substantial prior deformed substructures. Materials Characterization 151:429–435. https://doi.org/10.1016/j.matchar.2019.03.029

24. ASTM E8 / E8M - 16ae1 Standard Test Methods for Tension Testing of Metallic Materials. https://www.astm.org/Standards/E8. Accessed 15 Jun 2020

25. Oliver WC, Pharr GM (2004) Measurement of hardness and elastic modulus by instrumented indentation: Advances in understanding and refinements to methodology. Journal of Materials Research 19:3–20. https://doi.org/10.1557/jmr.2004.19.1.3

26. Sakai T, Belyakov A, Kaibyshev R, et al (2014) Dynamic and post-dynamic recrystallization under hot, cold and severe plastic deformation conditions. Progress in Materials Science 60:130–207. https://doi.org/10.1016/j.pmatsci.2013.09.002

27. Huang K, Logé RE (2016) A review of dynamic recrystallization phenomena in metallic materials. Materials and Design 111:548–574. https://doi.org/10.1016/j.matdes.2016.09.012

28. Sinclair CW, Mithieux JD, Schmitt JH, Bréchet Y (2005) Recrystallization of stabilized ferritic stainless steel sheet. Metallurgical and Materials Transactions A: Physical Metallurgy and Materials Science 36:3205–3215. https://doi.org/10.1007/s11661-005-0091-6

29. Bacroix B, Jonas JJ (1988) 1988—TextureMicro—The Influenceof Non-OctahedralSlip on Texture Development in FCC Metals.pdf. 267–311

30. Etter AL, Baudin T, Mathon MH, et al (2006) Stored energy evolution in both phases of a duplex steel as a function of cold rolling reduction. Scripta Materialia 54:683–688. https://doi.org/10.1016/j.scriptamat.2005.10.034

31. Ziouche A, Haddad A, Badji R, et al (2018) Microstructure, Corrosion and Magnetic Behavior of an Aged Dual-Phase Stainless Steel. Journal of Materials Engineering and Performance 27:1249–1256. https://doi.org/10.1007/s11665-018-3222-0

32. Lutterotti L, Matthies S, Wenk H-R (1999) MAUD: a friendly Java program for material analysis using diffraction

33. Lo KH, Shek CH, Lai JKL (2009) Recent developments in stainless steels. Materials Science and Engineering R: Reports 65:39–104. https://doi.org/10.1016/j.mser.2009.03.001

34. Gao XX, Liu HY, Wang YB, et al (2012) Effect of post weld heat treatment on microstructure and mechanical properties of stainless maraging steel weldments. Cailiao Rechuli Xuebao/Transactions of Materials and Heat Treatment 33:87–91. https://doi.org/10.4028/www.scientific.net/MSF.467-470.217

35. Badji R, Kherrouba N, Mehdi B, et al (2014) Precipitation kinetics and mechanical behavior in a solution treated and aged dual phase stainless steel. Materials Chemistry and Physics 1–9. https://doi.org/10.1016/j.matchemphys.2014.08.032

36. Kang JY, Kim H, Kim K Il, et al (2017) Effect of austenitic texture on tensile behavior of lean duplex stainless steel with transformation induced plasticity (TRIP). Materials Science and Engineering A 681:114–120. https://doi.org/10.1016/j.msea.2016.11.001

37. Wroński S, Tarasiuk J, Bacroix B, et al (2012) Investigation of plastic deformation heterogeneities in duplex steel by EBSD. Materials Characterization 73:52–60. https://doi.org/10.1016/j.matchar.2012.07.016

38. NISHIYAMA, Z (1934) X-ray investigation of the mechanism of the transformation from face centered cubic lattice to body centered cubic. Sci Rep Tohoku Univ 23:637

39. Von Giinter Wassermann in Berlin-Dahlem (1933) EinfluB der a-y-Umwandlung eines irreversiblen Nickelstahls auf Kristallorientierung und Zugfestigkeit. Archlv fUr das Eis enhiitt enwesen 42:

40. Wronski S, Ghilianu B, Chauveau T, Bacroix B (2011) Analysis of textures heterogeneity in cold and warm asymmetrically rolled aluminium. Materials Characterization 62:22–34. https://doi.org/10.1016/j.matchar.2010.10.002

41. Bacroix B, Schneider J, Franke A (2019) Evolution of recrystallization texture in non-oriented electrical steels during final annealing - Influence of shear stress after cold rolling. Journal of Physics: Conference Series 1270:. https://doi.org/10.1088/1742-6596/1270/1/012007

42. Wroński S, Wierzbanowski K, Bacroix B, et al (2009) Texture heterogeneity of asymmetrically cold rolled low carbon steel. Archives of Metallurgy and Materials 54:89–102

43. Wang YQ, Han J, Wu HC, et al (2013) Effect of sigma phase precipitation on the mechanical and wear properties of Z3CN20.09M cast duplex stainless steel. Nuclear Engineering and Design 259:1–7. https://doi.org/10.1016/j.nucengdes.2013.02.037

44. Pöhl F (2019) Pop-in behavior and elastic-to-plastic transition of polycrystalline pure iron during sharp nanoindentation. Scientific Reports 9:1–12. https://doi.org/10.1038/s41598-019-51644-5

45. Kheradmand N, Johnsen R, Olsen JS, Barnoush A (2016) Effect of hydrogen on the hardness of different phases in super duplex stainless steel. International Journal of Hydrogen Energy 41:704–712. https://doi.org/10.1016/j.ijhydene.2015.10.106

46. Ma I, Zhou C, Hen X, et al (2018) Effect of nitrogen on nanomechanical behavior of austenitic stainless steel investigated by nanoindentation. Materials Research Express 29:

47. Basa A, Barnoush A, Thaulow C (2012) Nanomechanical Testing of Hydrogen Effects on Super Duplex Stainless Steel. Mechanical Testing and Diagnosis 2:5–14

48. Tao P, Gong J ming, Wang Y fei, et al (2018) Characterization on stress-strain behavior of ferrite and austenite in a 2205 duplex stainless steel based on nanoindentation and finite element method. Results in Physics 11:377–384. https://doi.org/10.1016/j.rinp.2018.06.023

49. Argandoña G, Palacio JF, Berlanga C, et al (2017) Effect of the Temperature in the Mechanical Properties of Austenite , Ferrite and Sigma Phases of Duplex Stainless Steels Using Hardness ,Microhardness and Nanoindentation Techniques. Metals. https://doi.org/10.3390/met7060219

50. Ohmura T, Tsuzaki K (2007) Plasticity initiation and subsequent deformation behavior in the vicinity of single grain boundary investigated through nanoindentation technique. Journal of Materials Science 42:1728–1732. https://doi.org/10.1007/s10853-006-0885-y

51. Begau C, Hartmaier A, George EP, Pharr GM (2011) Atomistic processes of dislocation generation and plastic deformation during nanoindentation. Acta Materialia 59:934–942. https://doi.org/10.1016/j.actamat.2010.10.016

52. Ahn TH, Oh CS, Lee K, et al (2012) Relationship between yield point phenomena and the nanoindentation pop-in behavior of steel. Journal of Materials Research 27:39–44. https://doi.org/10.1557/jmr.2011.208

53. Xue KM, Wang Z, Wang X, et al (2020) Nano-indentation nanohardness and elastic modulus evolution of molybdenum processed by high-pressure torsion. Materials Science and Technology (United Kingdom) 0:1–9. https://doi.org/10.1080/02670836.2020.1740863

Declarations

Ethical approval

This study complies with the ethical standards set out by Springer. All the authors read and approved the final manuscript.

Funding

No funding was received for this work.

Conflicts of interest

The authors declare that there is no conflict of interest around the subject of the proposed paper.

Availability of data and material

The raw/processed data required to reproduce these findings cannot be shared at this time as they will be used in an ongoing study.

Code availability

Not applicable (jmp 13 design of experiments ‘free version’)

Figures

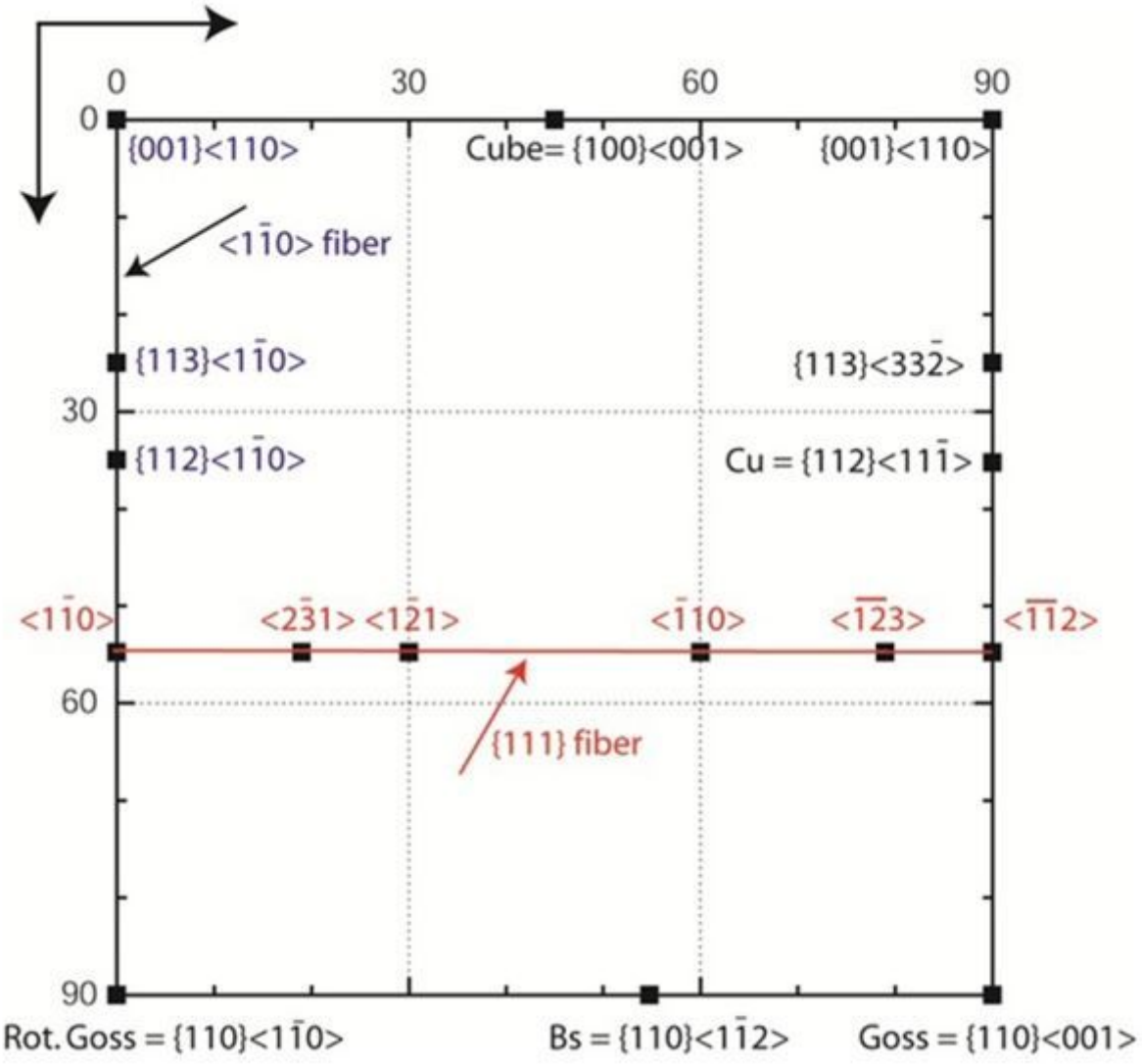

Figure 1

Main principal texture components for (bcc) and (fcc) metals after rolling or annealing in the φ2 = 45°section of the Euler space.

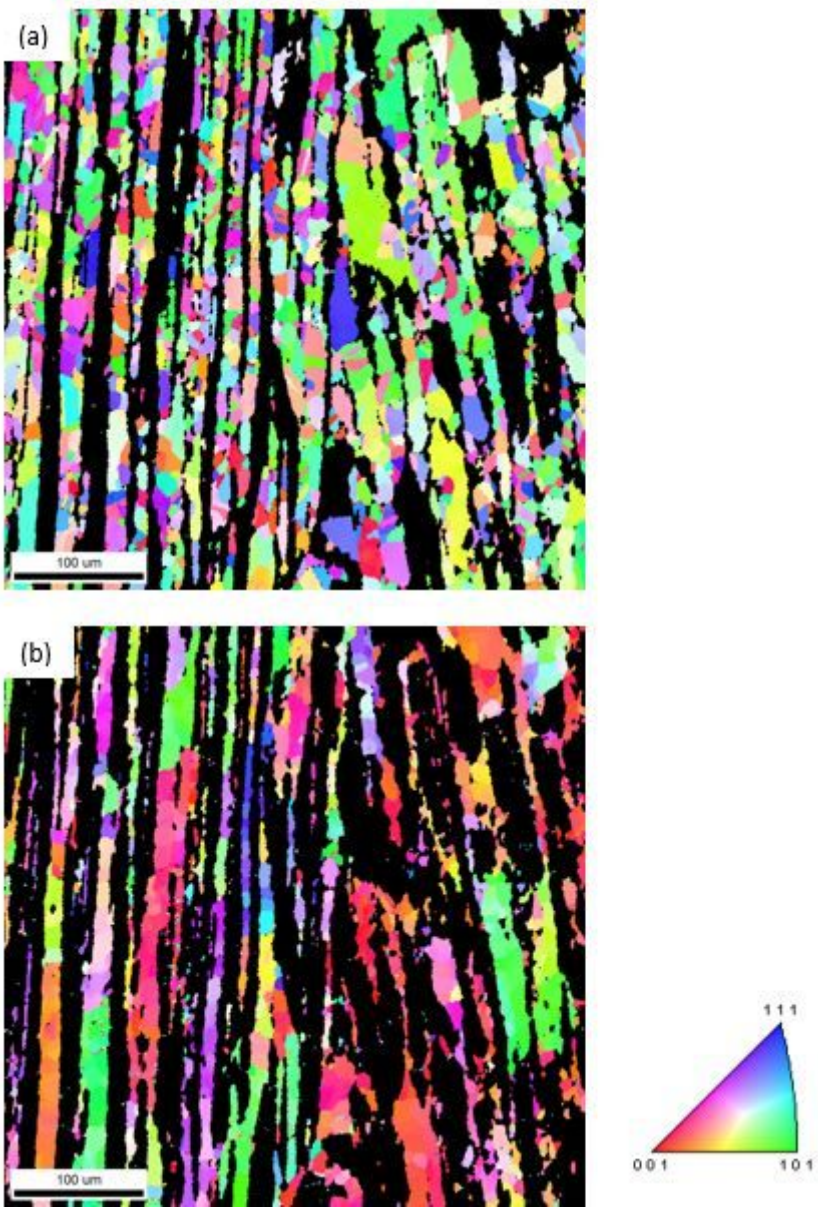

Figure 2

EBSD orientation maps measured at the as received state, a) austenite, b) ferrite.

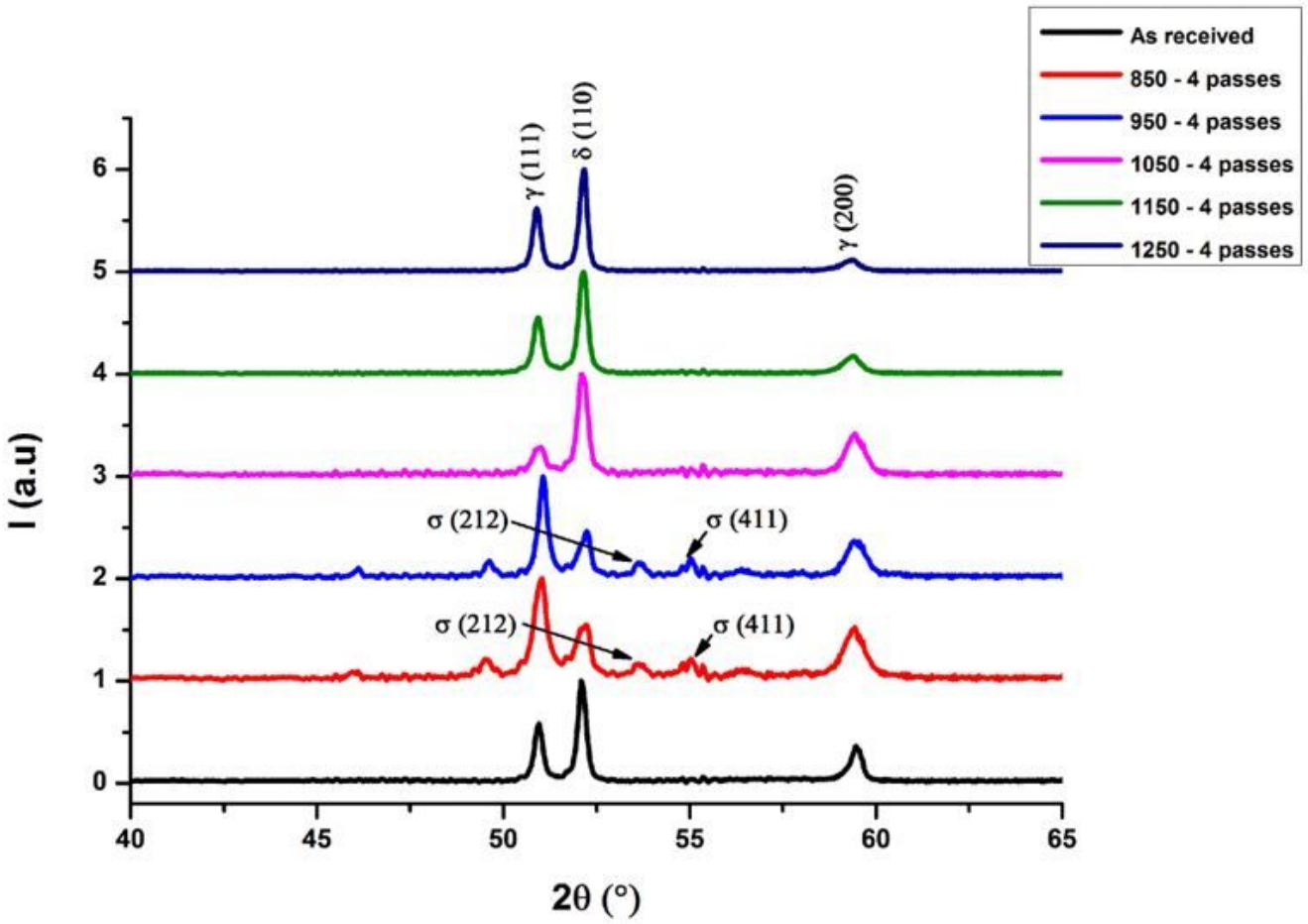

Figure 3

X-ray diffractogrammes obtained after 4 passes hot forging at different temperatures.

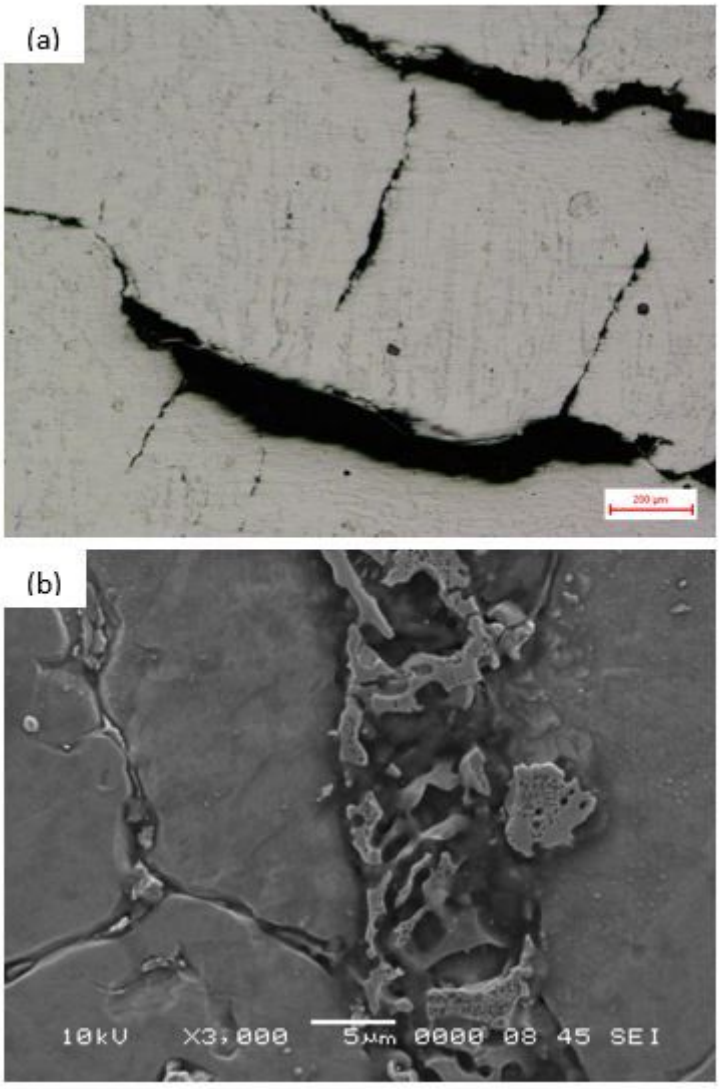

Figure 4

(a) Optical macrograph of the specimen hot forged at 850°C for 4-passes, (b) SEM micrograph showing the σ phase precipitation after 4-passes hot forging at 850°C.

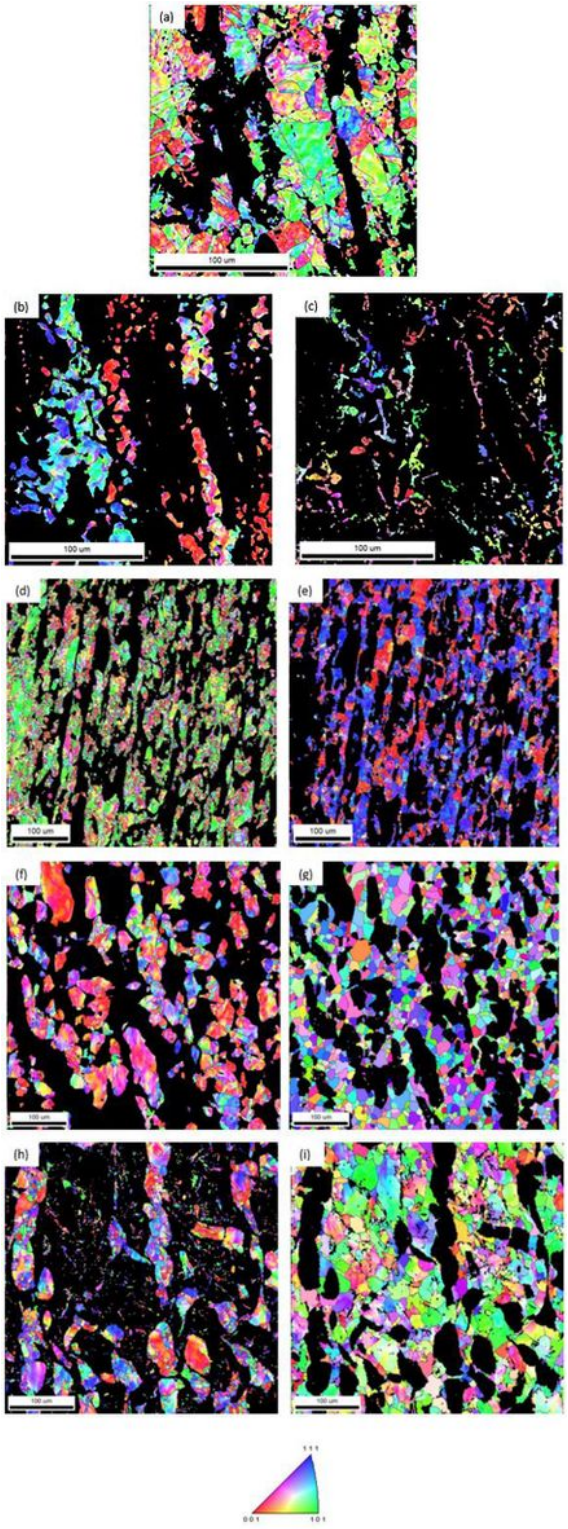

Figure 5

EBSD orientation maps after 4 passes hot forging for respectively: (a), (b) and (c) austenite, ferrite and sigma phase at 850°C, (d) and (e) austenite and ferrite at 1050°C, (f) and (g) austenite and ferrite at 1150°C, (h) and (i) austenite and ferrite at 1150°C.

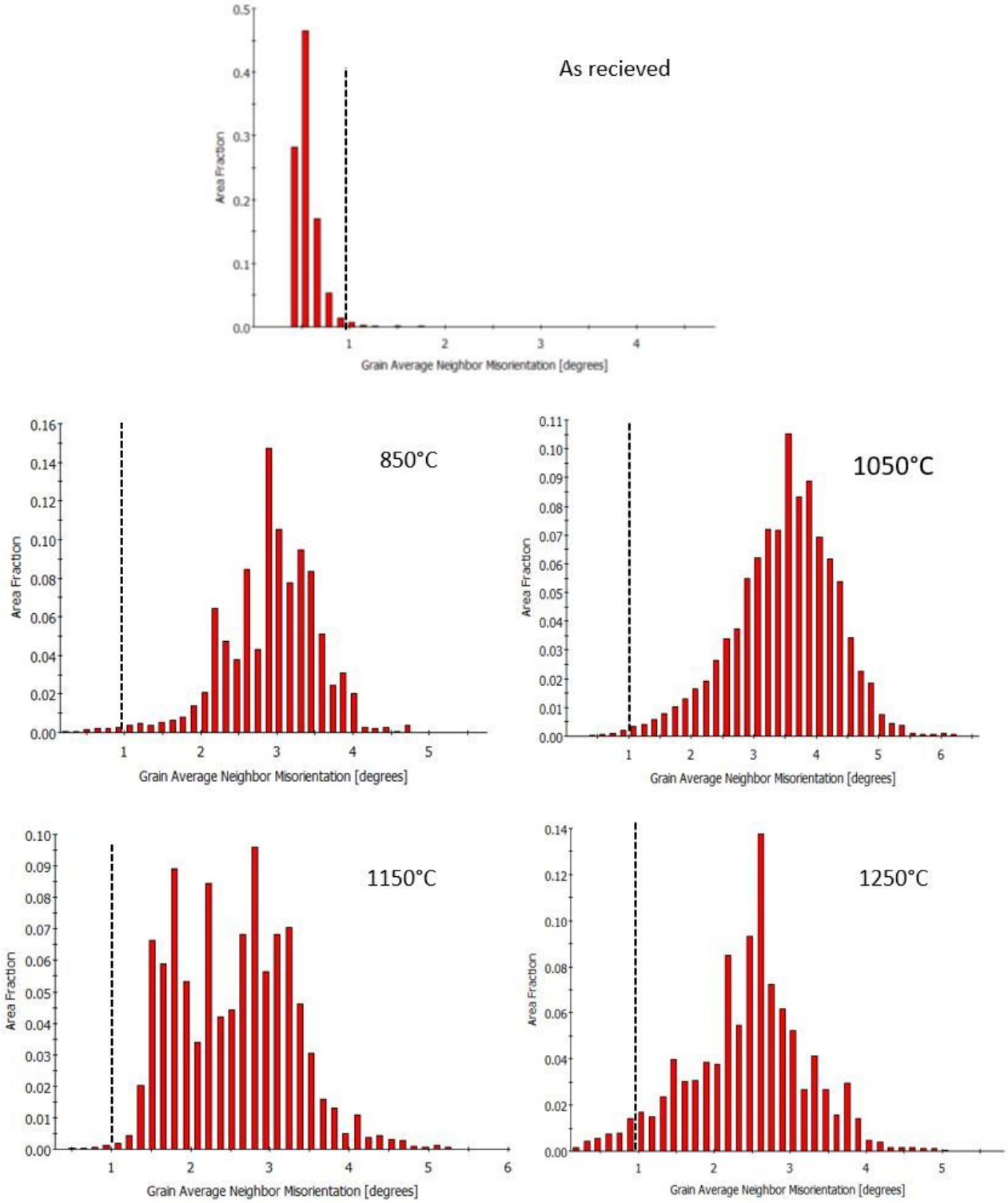

Figure 6

GAM profiles assessed for the austenite phase in the as received state and after hot forging at various temperatures. The black dashed line indicates the difference between recrystallized from deformed grains.

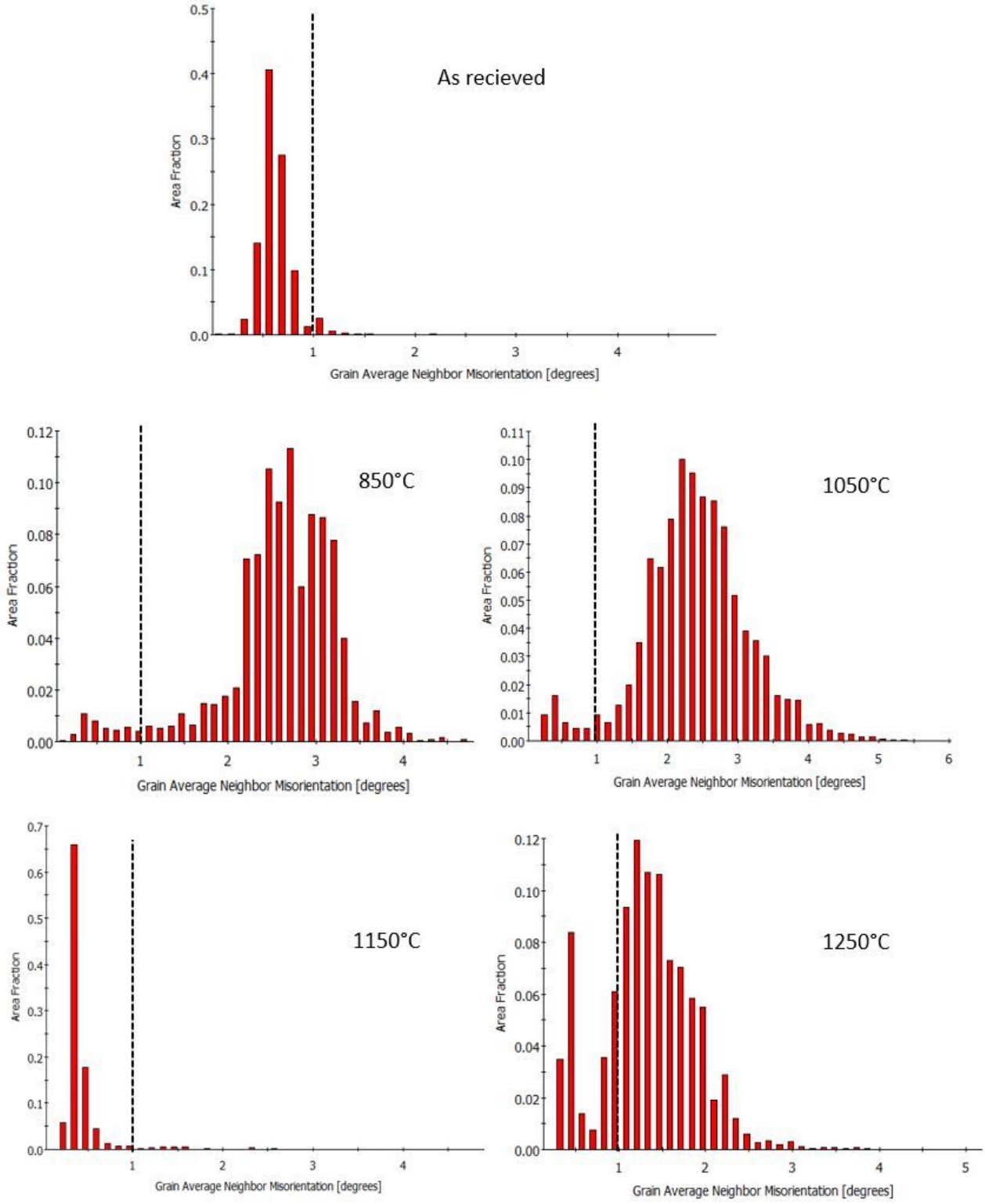

Figure 7

GAM profiles assessed for the ferrite phase in the as received state and after hot forging at various temperatures. The black dashed line indicates the difference between recrystallized from deformed grains.

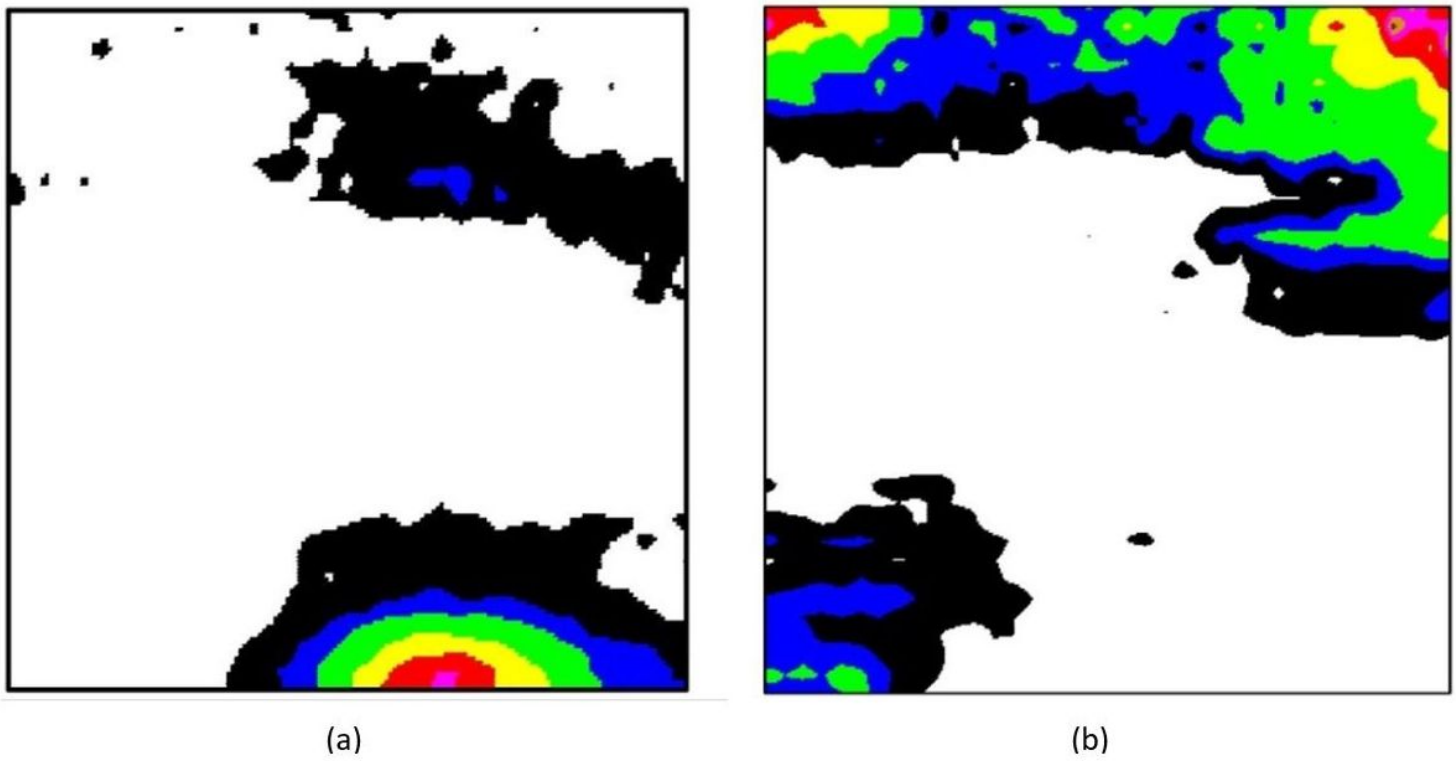

Figure 8

ODF (φ2 = 45°sections) measured at the as received state, (a) austenite and (b) ferrite

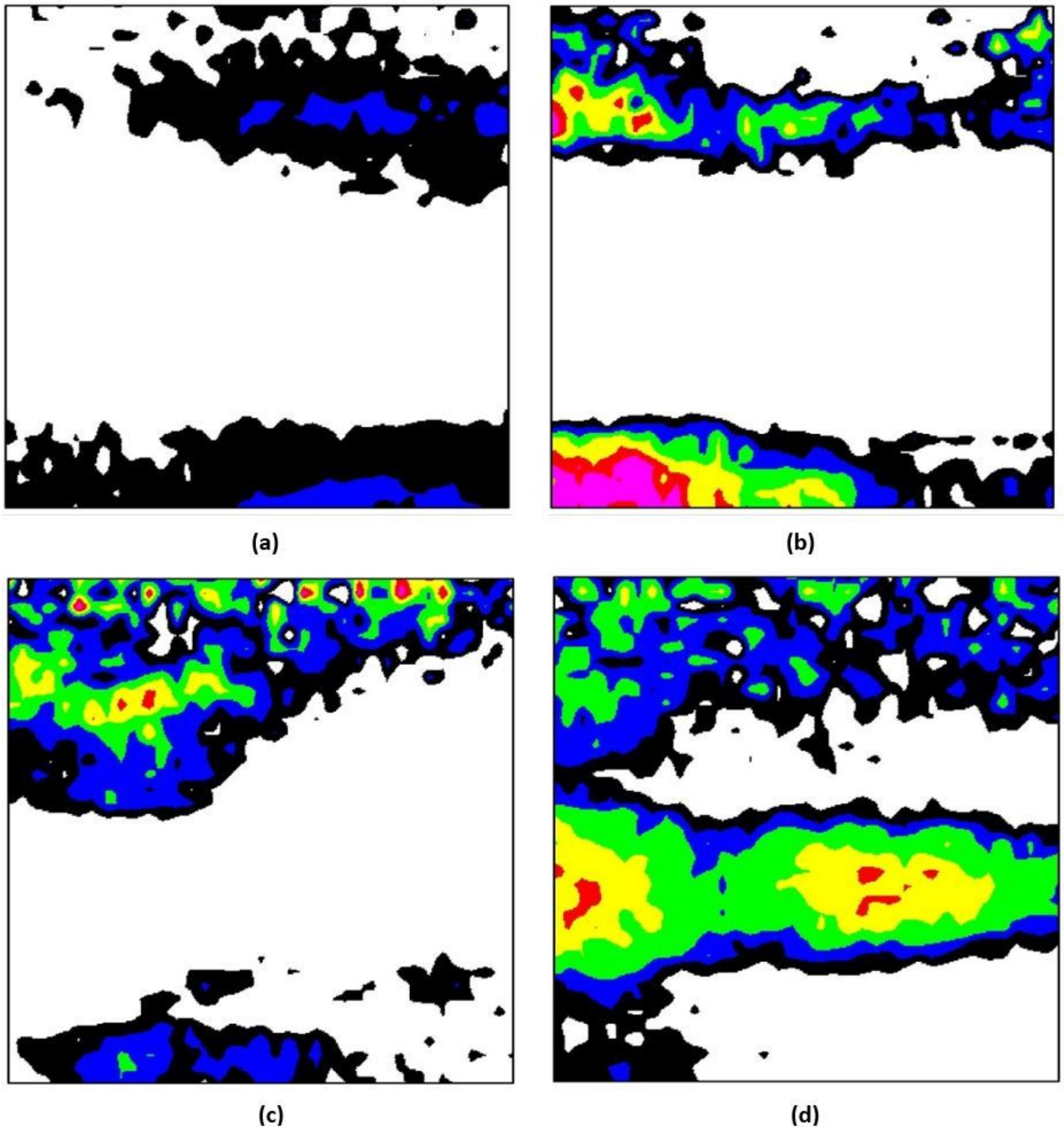

Figure 9

ODF (φ2 = 45°sections) of austenite after 4 passes hot forging at: (a) 850°C (b) 1050°C (c) 1150°C and (d) 1250°C

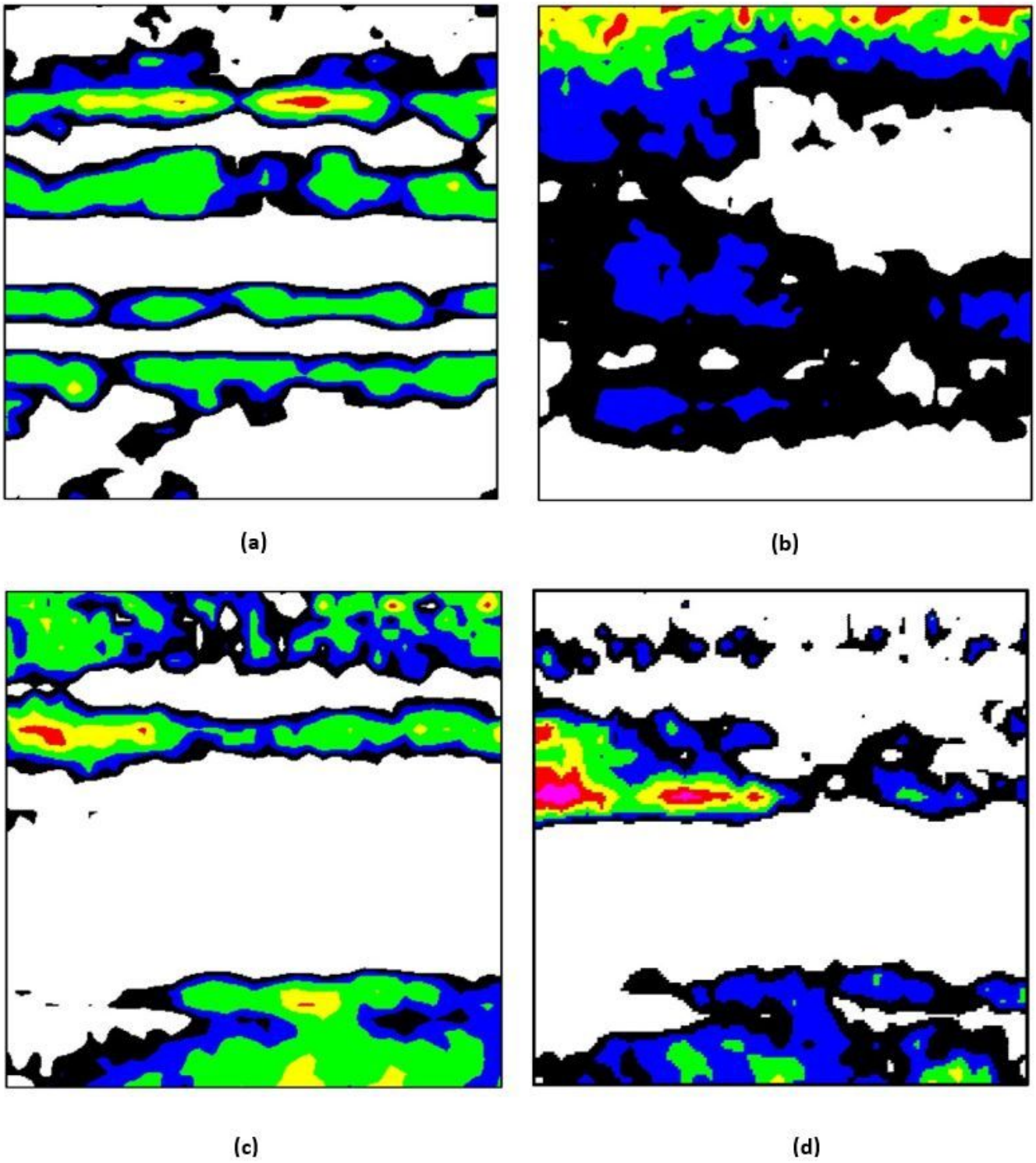

Figure 10

ODF (φ2 = 45°sections) of ferrite after 4 passes hot forging at: (a) 850°C (b) 1050°C (c) 1150°C and (d) 1250°C

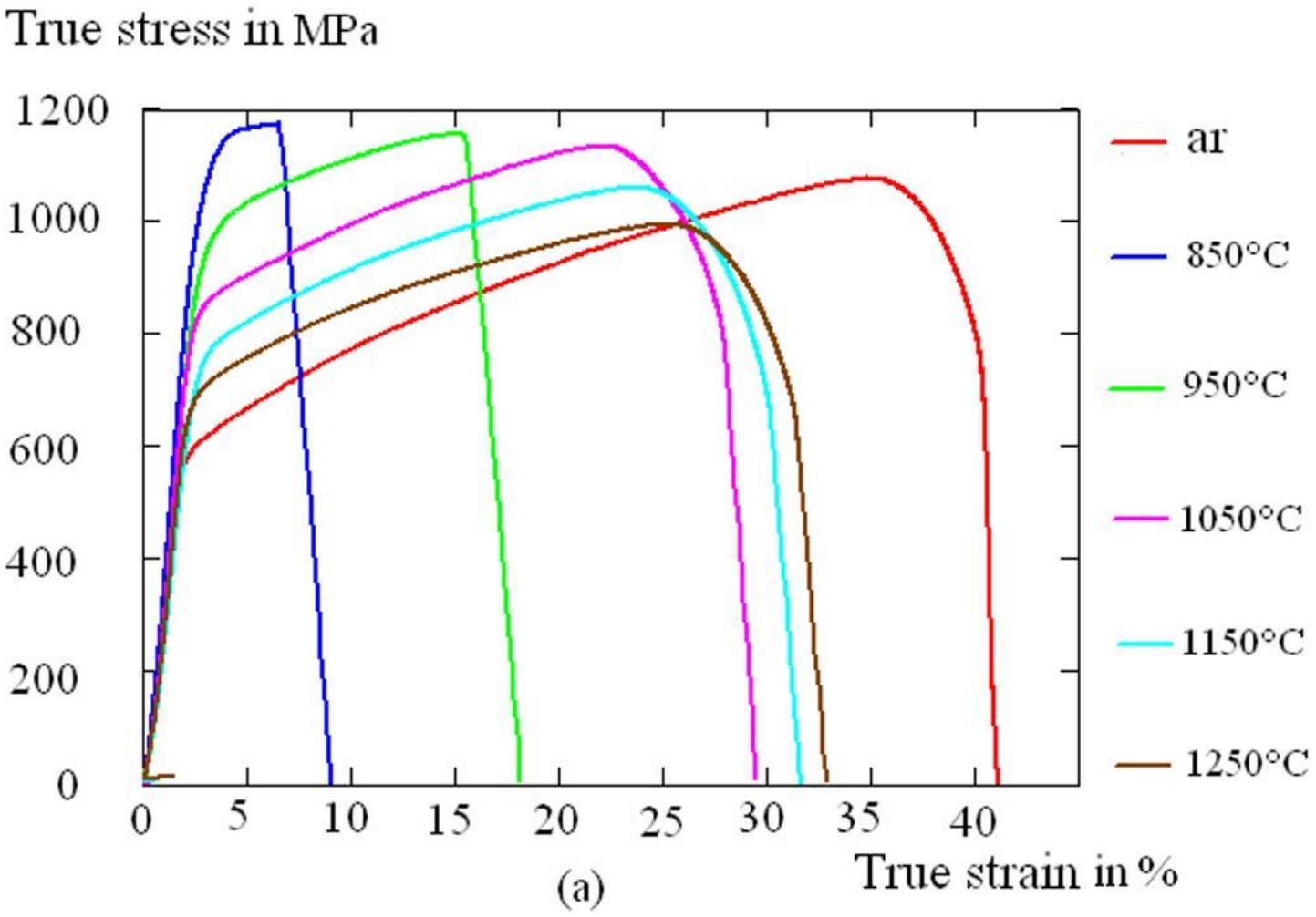

Figure 11

True stress-true strain curves after different forging temperatures.

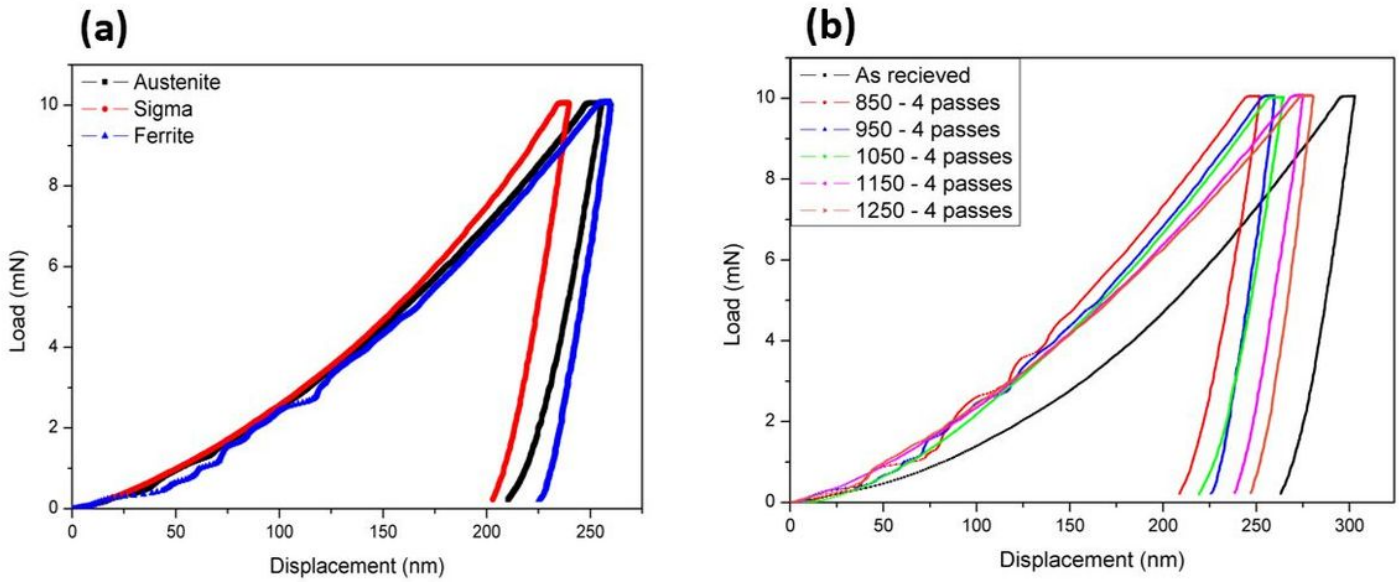

Figure 12

Nanoindentation load-displacement curves of samples obtained after 4 passes hot forging : (a) – P-h curves of different phases (ferrite, austenite and sigma phase) at 850° (b) –Conducted in ferrite phase of samples at different temperatures.

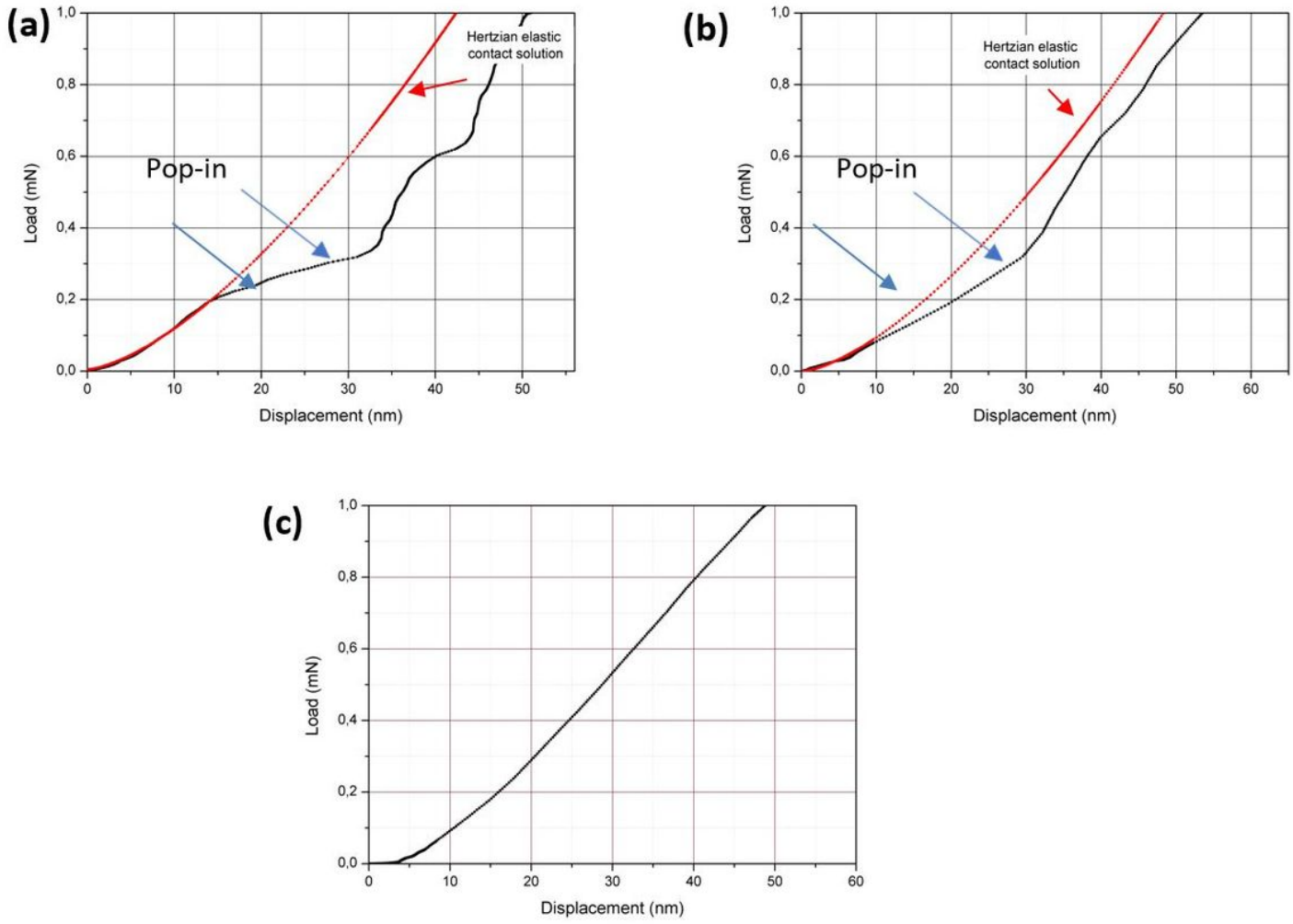

Figure 13

Zoom view of loading segment of P-h curves of Fig. 12b including Hertzian elastic contact solution for (a): as-received state, (b) and (c): those obtained after 4 passes hot forging at 850°C 1250°C respectively.